# MOLECULAR DYNAMICS SIMULATION USING HARD PARTICLES

M.P. ALLEN

*H.H. Wills Physics Laboratory, Royal Fort, Tyndall Avenue, Bristol BS8 1TL, United Kingdom*

D. FRENKEL

*FOM Institute for Atomic and Molecular Physics, PO Box 41883, 1009 DB Amsterdam, The Netherlands*

and

J. TALBOT

*Department of Chemistry, University of California, Los Angeles, Los Angeles, California 90024 USA*

1989

NORTH-HOLLAND–AMSTERDAM

**Contents**

1. Introduction . . . . . 304
2. MD vs. MC . . . . . 305
3. MD of hard spheres and related systems . . . . . 305
   3.1. Introduction . . . . . 305
   3.2. Simple hard sphere MD . . . . . 306
   3.3. Square-well atoms . . . . . 307
   3.4. Assemblies of atoms . . . . . 307
   3.5. Constant-pressure simulations . . . . . 308
4. MD of non-spherical molecules . . . . . 309
   4.1. Free-flight dynamics . . . . . 309
   4.2. Direct solution of collision equations . . . . . 310
   4.3. Retrospective detection of collisions . . . . . 311
   4.4. Collision dynamics . . . . . 315
5. Properties of interest . . . . . 316
   5.1. Introduction . . . . . 316
   5.2. Structure . . . . . 317
   5.3. Transport properties . . . . . 318
   5.4. Rotational dynamics . . . . . 319
   5.5. Elastic constants . . . . . 320
6. Hard lines . . . . . 321
7. Hard ellipsoids . . . . . 323
   7.1. Introduction . . . . . 323
   7.2. Computer code . . . . . 323
   7.3. Simulation parameters . . . . . 329
   7.4. Diffusion coefficients . . . . . 329
   7.5. Structure . . . . . 332
   7.6. Pretransitional dynamics . . . . . 333
   7.7. Elastic constants . . . . . 336
8. Hard spherocylinders . . . . . 338
   8.1. The smectic phase . . . . . 339
   8.2. Elastic constants . . . . . 343
   8.3. Collective rotation . . . . . 344
9. Hard dumb-bells . . . . . 345
   9.1. Computer code . . . . . 345
   9.2. Rigid vs. non-rigid molecules . . . . . 349
10. Look forward . . . . . 351
References . . . . . 351

Computer Physics Reports 9 (1989) 301–353
North-Holland, Amsterdam



# MOLECULAR DYNAMICS SIMULATION USING HARD PARTICLES

M.P. ALLEN

*H.H. Wills Physics Laboratory, Royal Fort, Tyndall Avenue, Bristol BS8 1TL, United Kingdom*

D. FRENKEL

*FOM Institute for Atomic and Molecular Physics, PO Box 41883, 1009 DB Amsterdam, The Netherlands*

and

J. TALBOT

*Department of Chemistry, University of California, Los Angeles, Los Angeles, California 90024, USA*

Received 19 December 1988

We review recent developments in the computer simulation of liquids and liquid crystals by molecular dynamics methods using hard particle models. We give a description of the computational methods involved, highlighting the special techniques needed for efficient detection of collisions between hard non-spherical bodies. We then summarize recent results in this field, dealing with structural and dynamical properties, as well as the interesting phase behaviour of some representative systems.

0167-7977/89/$18.55 

## 1. Introduction

In this review, we describe some recent progress made in the computer simulation of condensed matter using hard particle models. Computer simulations of classical many-body systems generally fall into two categories: molecular dynamics (MD), which amounts to the solution of Newton's equations of motion for a set of molecules, and Monte Carlo (MC), which is a method of sampling statistical ensembles using a random walk. In this article, we shall be most concerned with molecular dynamics.

The MD method has grown in popularity since the earliest work of Alder and Wainwright using hard spheres [1–4]. The increase in computer power that has taken place over the last 30 years has stimulated the development of more realistic potentials for use in simulations [5] and it is now even possible to adopt an ab initio approach to certain problems [6]. Nonetheless, there is still a strong case for studying the simplest potentials, particularly when it is desired to examine underlying principles rather than a specific molecular system. In such cases more insight may be gained from a simple model than from a complicated one. For atoms that are free to move (as distinct from a lattice gas) the simplest representation is the hard sphere model. The repulsive short-range interaction is taken to be a hard core of specified diameter $\sigma$; attractive forces are neglected completely. Simulations have helped to establish the importance of harsh repulsive effects in determining liquid structure [7], and provided the first quantitative test of the kinetic theory of dense fluids [8]; the discovery of long-time tails in certain time correlation functions [9] led to a complete overhaul of the underlying framework of this theory. Hard spheres have, for many years, functioned effectively as a reference system for atomic fluids. There is every reason to regard hard non-spherical bodies as being of comparable value in the molecular case: the essential shape of a molecule may be represented as a dumb-bell, a spherocylinder, or whatever. MC simulations of systems of this kind have been carried out for many years [10,11]; however, MD simulations have, until recently, been few and far between.

The study of hard *convex* bodies is of particular interest. For such systems, there are general formulae for the average pair-excluded volume and for other quantities that are required in kinetic theory and scaled particle theory [12,13]. There are no such general formulae for non-convex bodies. In fact, a much more general prescription exists for detecting the overlap of two convex bodies with given separation and orientation [14]. Furthermore, the equipotential surfaces of small molecules are usually convex, except at very high energies [15].

The resurgence of interest in the dynamical properties of these systems has been sparked by several developments. Firstly has come the discovery that hard molecules such as ellipsoids, and spherocylinders, can give rise to a rich variety of liquid crystalline phases [16]. Secondly, there have been significant advances in the kinetic theory of dense fluids of non-spherical bodies [17]. Thirdly, technical improvements is simulation approaches, and the steady increase in available computer power, have made such simulations feasible at only moderate expense.

In the following sections, we briefly review the respective advantages of molecular dynamics and Monte Carlo methods, and then outline the standard approach to MD of hard spheres. Next, we describe the possible approaches to efficient computer simulation of hard molecules, and we finish with a summary of some recent results in this field.

## 2. MD vs. MC

If one allows for the usual small differences between statistical ensembles, the results obtained from Monte Carlo and molecular dynamics simulations are broadly equivalent. In general, MC simulation algorithms are easier to write than MD ones, and this is particularly so in the case of hard particle models. However, there are some obvious advantages in using MD methods rather than MC. Firstly, of course, MD is essential if one is interested in dynamical properties such as time correlation functions, or relaxation to equilibrium. Secondly, for hard systems, MD is good for calculating structural and thermodynamic properties that characterize molecules in contact. Consider, for example, the calculation of the pressure, by straight constant-$NVT$ MC simulation (where $N$ is the number of particles, $V$ the volume and $T$ the temperature). This calculation requires the knowledge of the value of the pair distribution function at a distance and relative orientation where two molecules are just in contact. In practice, this part of the pair distribution function is evaluated by extrapolation. Of course, suitable alternative procedures exist to compute the pressure as a function of density [18], and conversely one can adopt constant-pressure MC simulation. Nonetheless, the pressure is calculated more directly via the collisional virial in MD. Other static, collisional, quantities, such as those associated with Enskog approximations to transport coefficients, are also most easily measured by MD.

On the question of which technique most efficiently explores configuration space, and promotes rapid equilibration, no general conclusion exists: the answer most certainly depends upon the precise system and state point under study, and in many cases also on the computer architecture and algorithms used. Even the question of what size of particle displacement gives the most efficient MC algorithm is not completely resolved. Evidence has emerged (see ref. [19] and references therein) that the best move-acceptance ratio may be lower than the frequently adopted 50%. Indeed, on a scalar computer, for hard systems, a sequential search for overlaps in a trial configuration may lead to rapid rejection of a move, and so it may be most efficient to work with a large particle displacement and an acceptance ratio as low as 10%. On a vector or parallel computer, however, where many tests must be carried out regardless, before a decision to accept or reject is taken, it may be better to work with a smaller particle displacement and thereby accept more moves.

A major attraction of MC methods is the ease with which one may probe different statistical ensembles, especially the grand canonical ensemble where particle numbers may vary. A good example of the power and flexibility of such MC techniques is the recent development of a technique to determine bulk phase coexistence properties [20]. During the past decade, much progress has been made in adapting MD algorithms to sample constant-temperature and constant-pressure ensembles for particles interacting with continuous potentials [21]. Recently it has been shown that this approach can also be made to work for hard systems [22]. We return to this point in section 3.5 below.

## 3. MD of hard spheres and related systems

### *3.1. Introduction*

When the molecular pair interaction is spherically symmetric, piecewise constant, with discontinuous changes at a small set of pair separations, the collisional dynamics may be solved

quite easily [1,2]. The simple hard sphere model is the prototype of this class, which also includes rough spheres and square-well molecules, as well as "discretized" versions of continuous potentials. In each case, free flight occurs between impulsive collisions. For each possible colliding pair of species $i$ and $j$, a quadratic equation must be solved for the time $t_{ij}$ to the next collision (if any):

$$|\boldsymbol{v}_{ij}|^2 t_{ij}^2 + 2(\boldsymbol{r}_{ij} \cdot \boldsymbol{v}_{ij}) t_{ij} + |\boldsymbol{r}_{ij}|^2 - \sigma^2 = 0, \tag{1}$$

where $\boldsymbol{r}_{ij} = \boldsymbol{r}_i - \boldsymbol{r}_j$ is the separation vector at zero time, $\boldsymbol{v}_{ij} = \boldsymbol{v}_i - \boldsymbol{v}_j$ is the relative velocity, and $\sigma$ is the pair separation at which the collision occurs (the atomic diameter in the simplest case of hard spheres). Only positive real roots $t_{ij}$ of eq. (1) correspond to real future collisions. The effect of a collision on particle velocities is determined by the laws of conservation of energy and of momentum $\boldsymbol{p} = m\boldsymbol{v}$, $m$ being the particle mass. In addition, there is the microscopic condition that the two surfaces in contact transmit the collisional impulse perpendicular to the common tangent plane: in other words, they are "smooth". For smooth hard spheres, denoting post-collisional values with primes, and setting $\boldsymbol{p}_{ij} = \boldsymbol{p}_i - \boldsymbol{p}_j$ the result is

$$\boldsymbol{p}_i' - \boldsymbol{p}_i = -(\boldsymbol{p}_j' - \boldsymbol{p}_j) = -\left(\boldsymbol{p}_{ij} \cdot \boldsymbol{r}_{ij}/\sigma^2\right)\boldsymbol{r}_{ij}. \tag{2}$$

Rough spheres [23–27] differ in that the molecules possess angular velocity, have a moment of inertia, and obey a different rule for transmitting the collisional impulse. Post-collisional values are determined by the laws of conservation of energy, and of linear and angular momentum, together with the microscopic condition of roughness. In each case, the dynamics proceeds from one collision to the next. In this section we describe the approach used to solve the collision equations for systems of this kind.

### *3.2. Simple hard sphere MD*

The method used to carry out hard sphere MD has changed very little from that described originally by Alder and Wainwright [2]. The usual procedure for hard sphere simulations is to solve the collision time equation, eq. (1), for each possible colliding pair of atoms. Usually an up-to-date list of forthcoming collisions is maintained by the program. The earliest collision time is located by searching the list, and the atomic configuration is advanced in time, using free-flight Newtonian dynamics, to the point of collision. The collision dynamics are then implemented for the colliding pair: the conservation laws determine the post-collisional velocities in terms of the pre-collisional values and the impact parameters, according to eq. (2).

Following this, the collision lists are updated. This entails calculating collision times for the just-collided pair, and also re-examining the fate of all atoms which would have met either one of this pair, had they not met each other first. Then a search is started for the next collision, and the process is repeated. Further details of the hard sphere MD technique can be found elsewhere [2,28,29].

The simulation proceeds collision-by-collision, rather than step-by-step as in MD using continuous potentials. Two time-consuming operations can be identified: calculating collision times for atom pairs, and updating the collision lists. The collision time calculation will involve

many pairs but the basic process is quite efficient, since the atomic centres move in straight lines and the collision time equation (eq. (1)) is quadratic. Lists based on neighbour distances [28,30] or on a spatial cell structure [31,32], similar to those used for continuous potentials, can be used to improve program efficiency. For small systems quite simple procedures are satisfactory for maintaining the collision lists, but as the system size grows it becomes more important to optimize this part of the program. An elegant tree-structure approach for handling the collision sequence has been described [33]. The same approaches may be used in the simulation of large systems and hard non-spherical molecules. Schemes for large-scale simulations on vector and parallel computers are described elsewhere [34]. We shall not discuss these particular problems any further.

One point perhaps should be stressed. In periodic boundaries, the search for the next collision partner is usually restricted to minimum image neighbours. However, there is no guarantee that the next collision will in fact involve a particle that was a nearest image at the time the search was conducted. For low-density systems in particular, the times between collisions may become long, and a particle may traverse many box lengths before colliding. This possibility was considered by Frenkel and Maguire in their simulations of hard line segments (see ref. [35] and section 6) but applies equally to hard spheres and all the other systems considered here. A simple way to handle the matter is to completely recalculate the collision lists involving a particle, just as if it had suffered a collision, if it moves in free-flight a distance $(L/2 - \sigma)/2$ (where $L$ is the simulation box length) in any direction. Thus, no particle can move relative to another by more than $L/2 - \sigma$ before it is re-examined. These events can be fitted into the collision-list scheme described above with little difficulty.

### 3.3. Square-well atoms

The molecular dynamics of atoms interacting via a square-well potential may be carried out in a manner analogous to that used for hard spheres [2]. Collisions with the inner hard core are handled exactly as described above. At the outer boundary, there are various possibilities. For collisions in which the square well is entered from outside, the basic conservation laws generate post-collisional velocities, with the drop in potential energy converted into extra kinetic energy for the newly-formed pair. When a pair hits the outer well barrier from the inside, either escape or an internal bounce collision occurs, depending upon the collision parameters. The search for future collisions, and the handling of collision lists, are carried out just as efficiently as for simple hard spheres.

### 3.4. Assemblies of atoms

Anticipating the next section, the principal difficulty with the simulation of hard non-spherical molecules is that the free-flight dynamics, although exactly known, generate a transcendental equation for the time of collision between two bodies. This is because, in addition to rectilinear translation, rotation occurs about the centre of mass, and also because the colliding particle surfaces are, in general, non-spherical. The treatment of non-rigid molecules, for which the exact equations of motion are more complicated, is even more uninviting. These problems may be circumvented by a natural extension of the hard sphere and square-well approach: molecules are

built up out of atomic hard spheres [36,37]. The bonds between atoms in a molecule are not rigid, but take the form of narrow square wells, with infinite potential barriers; thus the bond lengths are constrained to "rattle" within rigid pre-defined limits. The dynamics is still that of atomic free flight between collisions, and so the basic collisional problem is very simple, and cheap to solve. There is a trade-off however: the more precisely defined are the bond lengths, the more computer time is spent on frequent intramolecular collisions, rather than on the more interesting intermolecular ones. Nonetheless, investigations have shown this approach to be very cost-effective, and many properties of the model are very close to those of the limiting ideal rigid molecule, as determined by MD [38] or MC [39]. We shall return to these points in section 9. Of course, a natural advantage of this approach is its ability to treat flexible molecules without any additional complications [36,37].

### 3.5. Constant-pressure simulations

In the discussion so far we have implicitly assumed that the MD simulations have been performed in the microcanonical constant-*NVE* ensemble. While this is the most convenient choice from the computational point of view, there is some interest in extending the MD technique to other ensembles, particularly for the study of phase transitions.

Andersen has proposed a Lagrangian formalism, yielding modified equations of motion for performing MD simulations at constant pressure [21]. In the method for the isobaric-isoenthalpic (constant-*NPH*) ensemble, the volume $V$ of the simulation box is a dynamical variable that fluctuates in response to imbalances between the internal and external (constant) pressures. Corresponding to the volume is a "mass" $M$ (its dimensions are actually mass/length$^4$), which influences the dynamic but not the structural properties. The choice of $M$ is, to an extent, arbitrary, but guidelines exist [21].

In three dimensions the Andersen Lagrangian is

$$\mathscr{L}(\boldsymbol{q}, \dot{\boldsymbol{q}}, V, \dot{V}) = \tfrac{1}{2}mV^{2/3}\sum_{i=1}^{N}\dot{\boldsymbol{q}}_i\cdot\dot{\boldsymbol{q}}_i - \sum_{i>j}u\left(V^{1/3}\,|\boldsymbol{q}_i-\boldsymbol{q}_j|\right) + \tfrac{1}{2}M\dot{V}^2 - PV, \tag{3}$$

where $\boldsymbol{q}_i$ are scaled coordinates lying in the unit cube, $m$ is the particle mass, $u(r)$ is the pair potential and $P$ is the external pressure. The real positions and momenta are given by $\boldsymbol{r}_i = V^{1/3}\boldsymbol{q}_i$ and $\boldsymbol{p}_i = mV^{1/3}\dot{\boldsymbol{q}}_i$, respectively. The equations of motion for hard spheres in the constant-*NPH* ensemble have been derived by De Smedt et al. [22]. Between collisions the scaled momenta $\boldsymbol{\pi}_i = \boldsymbol{p}_iV^{1/3}$, are constant,

$$\dot{\boldsymbol{q}}_i = \boldsymbol{\pi}_i/mV^{2/3}, \qquad \dot{\boldsymbol{\pi}}_i = \boldsymbol{0}, \tag{4}$$

and the system volume evolves according to the differential equation:

$$M\ddot{V} = -P + \tfrac{2}{3}V^{-5/3}\sum_{i=1}^{N}\frac{\boldsymbol{\pi}_i^2}{2m}. \tag{5}$$

At a collision between spheres $i$ and $j$ the scaled momenta and volume derivative change discontinuously:

$$\pi_i' - \pi_i = -(\pi_j' - \pi_j) = \delta_c V^{2/3}(q_i - q_j)/\sigma \tag{6}$$

and

$$\dot{V}' - \dot{V} = \frac{\delta_c \sigma}{3MV}, \tag{7}$$

where primes denote post-collisional values and

$$\delta_c = -\frac{(\pi_i - \pi_j)\cdot(q_i - q_j)/\sigma + \sigma m\dot{V}/3V}{1 + m\sigma^2/18MV^2}. \tag{8}$$

Since $\delta_c$ is positive a collision always increases $\dot{V}$, while the particle kinetic energies decrease or increase depending on whether the box was expanding or contracting at the time of collision.

De Smedt et al. [22] tested this method for the one-dimensional system of hard rods. To our knowledge no simulations of hard spheres in the constant-*NPH* ensemble have so far been attempted. However, although the equations of motion are more complex than those for hard spheres at constant volume, this should not be a great deterrent. By applying the methods described in section 4, the procedure may be extended in a straightforward way to hard non-spherical bodies. Moreover, the collision equations remain valid when a soft potential is added to the hard core.

## 4. MD of non-spherical molecules

### *4.1. Free-flight dynamics*

We assume that the molecules move freely between collisions. This implies rectilinear motion of the centre of mass of each molecule, and rotation about the centre of mass with constant angular momentum. For the cases discussed here (rods, ellipsoids, spherocylinders, dumb-bells), the molecules are axially symmetric, and we treat them as linear rotors. End-over-end rotation occurs, with the angular velocity perpendicular to the symmetry axis, and with a single value of the moment of inertia $I$; angular velocity $\omega$ and angular momentum $J$ are related by $J = I\omega$. There is no moment of inertia and no angular velocity about the symmetry axis. This is not the only possible choice: an alternative would have been to treat the molecules as symmetric tops and allow rotation about the symmetry axis. However, when we consider the nature of the collisions between molecules, treating the colliding surfaces as perfectly smooth, it becomes clear that, for each molecule, the component of angular velocity along the symmetry axis will be conserved. Consequently, it is sensible, and simpler, to adopt the linear rotor model.

For linear rotors, both linear and angular velocity vectors are constant between collisions. Consider a molecule $i$. The unit vector along the symmetry axis, $u_i$, rotates in a plane

perpendicular to the angular velocity vector $\omega_i$. This motion is easily described in a coordinate system based on $\boldsymbol{u}_i$, $\hat{\omega}_i (= \omega_i / |\omega_i|)$ and $\hat{\omega}_i \times \boldsymbol{u}_i$, evaluated at some initial time $t_1$. The FORTRAN code for advancing the molecular position and orientation to a later time $t_2$ is:

```
DT = T2 - T1

RXI = RXI + VXI * DT
RYI = RYI + VYI * DT
RZI = RZI + VZI * DT

OMT = OMI * DT
COSOMT = COS(OMT)
SINOMT = SIN(OMT)
OUX = OYI * UZI - OZI * UYI
OUY = OZI * UXI - OXI * UZI
OUZ = OXI * UYI - OYI * UXI
UXI = UXI * COSOMT + OUX * SINOMT
UYI = UYI * COSOMT + OUY * SINOMT
UZI = UZI * COSOMT + OUZ * SINOMT
```

We find it convenient here to store the unit vector $\hat{\omega}_i$ in variables OXI, OYI, OZI, and the magnitude $|\omega_i|$ separately in OMI. Centre-of-mass positions, velocities, and axis unit vectors are stored in correspondingly named FORTRAN variables (RXI, RYI, RZI), (VXI, VYI, VZI) and (UXI, UYI, UZI).

### *4.2. Direct solution of collision equations*

As has been mentioned above, the dynamics of non-spherical molecules generates a transcendental equation for the time at which collision occurs. We require an "overlap" function $f_{ij}(t)$ of the time $t$, which also depends implicitly on the initial positions, velocities etc. of two particles $i$ and $j$. The form of the function reflects the shape of the molecules: it should be zero when the two molecules are in contact, and should change sign as the molecules move through contact. The term "overlap" is used with some licence here: some of the models of interest actually possess zero pair-excluded volume, and so never overlap. Particular forms of $f$ are discussed below, when we turn to specific models. In any case, we are searching for positive real roots $t = t_{ij}$ of the equation

$$f_{ij}(t) = 0, \tag{9}$$

which is the generalization of eq. (1). We wish to solve such equations efficiently and reliably: missed collisions could cause problems. A standard approach to solving algebraic equations involves combining the Newton–Raphson method with interval bisection [40]. For the Newton–Raphson method, we also require the time derivative of $f$. An example of computer code, for hard dumb-bells, appears in section 9.1. Irrespective of the exact method, however, the

search for a root truly begins only when it has been bracketted within a finite time interval, and this is the major computational challenge.

To prevent the search for roots being totally open-ended, it is convenient to enclose each molecule in a circumscribing sphere and to seek collisions only while the spheres overlap: this means solving an equation like eq. (1) so as to define the time interval of interest. We are still left with the problem of locating sub-intervals of time in which collisions can be shown either to occur (i.e. in which $f$ changes sign) or not to occur. This latter objective poses significant technical difficulties. Near-grazing collisions will cause the function $f(t)$ to approach zero arbitrarily closely; in an actual grazing collision, eq. (9) will have two very close roots as the function $f(t)$ briefly changes sign and goes back again. Following a collision, a rapid re-collision of the same two molecules may occur (in contrast to the hard-sphere case, for example) and it is essential not to miss this kind of behaviour.

For the special case of hard line segments [35] it is possible to develop a procedure which, for a given pair of molecules, rigorously excludes roots of the collision equation from a certain interval of time. This allows the computer program to advance in time, bracketting and then locating precisely every collision. The details of the method are explained fully in ref. [35]. Although the approach of ref. [35] could, in principle, be extended to arbitrary hard-core molecules, the method tends to become cumbersome. The obvious alternative is to calculate the function $f$ for each pair of molecules many times, at regular intervals during the period of overlap of the circumscribing spheres, and look for sign changes. This entails acceptance of the possibility that a small fraction of the grazing collisions will be missed. In any case, it is useful to check all pairs for overlap (if this can occur) at intervals, to guard against mistakes; also, for models of the hard line type, the observed collision frequency can be compared with an exactly calculable value.

To our knowledge, very few simulations involving direct solution of the collision equations have been carried out. Bellemans and coworkers [38] conducted some preliminary simulations of hard dumb-bells in two dimensions; an MD simulation of three-dimensional dumb-bells has appeared recently [41]. Further work on hard lines and related systems has also been carried out [42–44] (se also section 6).

### *4.3. Retrospective detection of collisions*

We have introduced above the idea of calculating the collision function $f$ for each pair at regular intervals, and looking for sign changes: this allows the program to bracket a root of the collision equation before homing in on the exact solution. A development of this approach was first applied by Rebertus and Sando to hard spherocylinders [45]. Most of our results have been obtained using this method, and so we shall go into some detail in describing the technicalities.

The molecular configuration is advanced on a regular step-by-step basis, just as in standard continuous-potential MD, but using free-flight without collision. At the end of each step, the configuration is examined for overlapping pairs of molecules. For each overlapping pair, the collision equation is solved retrospectively to find the time at which collision should have occurred. The system is rewound to the point of collision, collision dynamics implemented, and the system run forward again to the end of the step. The expensive part of this, the search for overlaps, is readily vectorized or parallelized. This is the significant technical point: the routine

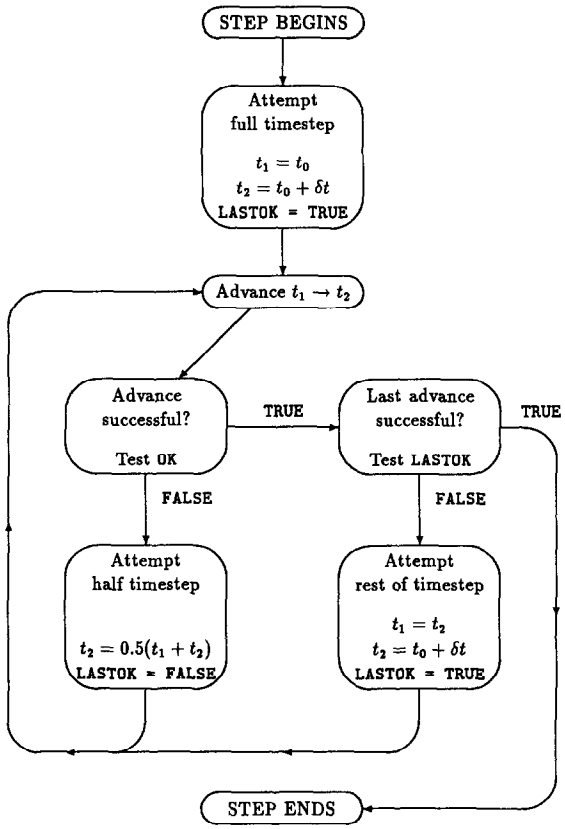


Fig. 1. Flow diagram for a timestep in a molecular dynamics program using retrospective detection of overlaps.

to search the configuration for overlaps is very much like the central loop of conventional simulation programs. The complicated (although not very time-consuming) part consists of handling multiple overlaps and resolving sequences of (possibly) inter-dependent collisions occurring within a very short time of each other.

The flow diagram in fig. 1 and the section of computer code below, show the way in which our main program handles this task.

```
DO 1000 STEP = 1, NSTEP

    T0 = REAL(STEP - 1) * DT
    T1 = T0
    T2 = T0 + DT
    LASTOK = .TRUE.

100     CALL ADVANC(T1, T2, OK)

    IF (OK) THEN
```

```
            IF (LASTOK) GOTO 500
            T1 = T2
            T2 = T0 + DT
            LASTOK = .TRUE.
            GOTO 100

        ELSE

            T2 = 0.5D0*(T1 + T2)

            IF ((T2 - T1).LT.EPS) THEN

                PRINT*, 'TIME INTERVAL TOO SMALL'
                STOP

            ENDIF

            LASTOK = .FALSE.
            GOTO 100

        ENDIF

    500 CONTINUE

    ...update neighbour lists at intervals
    ...output results at intervals

    1000 CONTINUE
```

Within a loop over timesteps, the program advances the configuration from time $t_0$ to time $t_0 + \mathrm{d}t$ incorporating all collisions correctly (apart from a very small number of grazing collisions which are not detected). The ADVANC routine attempts to advance the configuration from an initial time $t_1$ to a final time $t_2$ incorporating all collisions correctly. If this is accomplished without difficulty, it returns as TRUE the logical flag OK; otherwise OK is set FALSE. The main routine keeps track of OK and the flag LASTOK, which records whether or not the last attempt at advance was successful or not. By coding the main program in this way, we can allow the ADVANC routine to be quite simple, catering for the overwhelming majority of cases (for a suitably chosen interval $\mathrm{d}t$) in which a single collision or a small number of non-interfering collisions occurs during a time step. Whenever ADVANC is unable to resolve the collisions unambiguously, it sets OK to be FALSE and returns with the configuration unmoved at time $t_1$. Following this, the program simply halves the timestep, records the fact that a failure occurred, and tries again. If the timestep becomes too small to be handled satisfactorily due to roundoff errors ((T2 – T1).LT.EPS above, where EPS is a small constant) then the program terminates with an error message. When an advance is successful, the program tries to cover the

remainder of the timestep in a single go, and the process continues. A timestep is completed when two successive advances produce an OK result, or when the very first advance covers the whole step in one.

Within the advance routine the procedure is as follows. The initial configuration at time $t_1$ is stored, and all molecules are moved forward to the new time $t_2$. A search for overlapping pairs is made, and a list of these constructed. If there are any overlaps, the collision equation is solved for each such pair. Specifically, we look for roots of the equation $f_{ij}(t) = 0$ as in the previous section, but in the certain knowledge that at least one such root exists within the prescribed time interval. The pair collisions are sorted into chronological order. Any secondary collisions (collisions involving atoms $i$ and $j$, either of which have been involved in a collision appearing earlier in the list) are removed. The collisions are then examined in order of occurrence. For each collision, the colliding pair $i$ and $j$ are moved back to the point of collision, allowed to collide, and moved forward again to time $t_2$. They are then examined to see if, after this, they overlap with any other molecules. If such an overlap is detected then the step is immediately abandoned: the original configuration (at time $t_1$) is restored, the flag OK set to FALSE and the routine returns. The reason for this quick rejection is explained below. If no overlap is detected, the routine goes on to consider the next colliding pair, and so on through the whole list. The collision list is typically quite short: almost always less than ten collisions per step in our simulations, and often just two or three. If all collisions on the list are tackled successfully, the OK flag is set and the system moved to time $t_2$.

In this way, we may be confident in the results of the routine given an OK return; if there is any complexity at all in the sequence of collisions then OK is set to FALSE. The reason for this is that such events are infrequent. They are handled (following a failed return) when the timestep is reduced in the leftmost branch of the flow diagram. Thus, we may take two or more sub-steps, each involving a call to the advance routine, to cover a single timestep $\mathrm{d}t$. The main disadvantage of this simple approach is that it becomes less efficient as the system size increases. This is because a "local" problem (a complicated collision sequence involving a few close particles) triggers a "global" response (the rewinding of the whole configuration and shortening of the timestep, followed by an additional complete search for overlaps). For simulation of large systems ($N > 500$) slightly more complicated programming is required to resolve such situations; however, this problem does not arise for the small systems discussed here. As measured by the average length of sub-steps covered successfully by the advance routine, relative to the input timestep $\mathrm{d}t$, we run the program at an efficiency of order 75–85%.

One or two additional technical points should be mentioned. For reasons similar to those discussed in the previous section, the first action undertaken by the advance routine is to examine molecular velocities and check that no pair of molecules could move relative to one another by half a box length minus their own diameter, in any coordinate direction, during the interval $t_2 - t_1$. If the configuration fails this test, OK is set FALSE and the routine returns. Secondly, in solving the collision equations, an absolutely foolproof method such as the combined Newton–Raphson/bisection algorithm must be used [40]. Finally, we speed up the pair searching by the use of a Verlet neighbour list [30]. This is more convenient than a cell-structure, since it may be made to reflect the molecular shape, which in our case is quite anisometric. We are already using a function $f$ which signals the overlap of two molecules. By changing a parameter in this function, we may in general turn it into a new function $f_{\mathrm{list}}$, which

indicates when two convex bodies, with a larger excluded volume than the original molecules, overlap. We construct our Verlet-type lists using $f_{\text{list}}$ to decide whether or not two molecules are neighbours, rather than employing the usual criterion of distance between the centres. This approach works well in the dense liquid state, where neither translation nor rotation occur particularly quickly.

The list is updated at regular intervals, but the program includes a "safety skin depth" check, based on yet another version of the $f$ function, to warn when molecules not on the neighbour list are penetrating too far into the neighbourhood region between updates. This acts as a trigger for automatic reduction of the update interval. Construction and use of the Verlet list are vectorizable on a supercomputer which supports "gather" and "compress" operations. Computer code to illustrate these points for hard ellipsoids appears in section 7.2.

Although the details we have outlined above may be new, we should emphasize that we are not the first to use this type of simulation technique involving the retrospective handling of collisions. The basic method is suitable for a wide variety of applications, including the original work on hard rigid molecules [45], the application of strict "windows" on internal degrees of freedom of flexible molecules [46] and (by replacing free-flight dynamics with standard continuous-potential MD) combinations of hard and soft potentials [47]. In sections 6–9, we discuss various results that we have obtained using this approach.

### 4.4. Collision dynamics

In the previous sections we have described the method by which a collision may be located. The program must then implement the collision dynamics, which are determined by the conservation laws of energy, linear momentum and angular momentum, and also (in the cases of interest here) by the condition that the colliding surfaces are smooth.

Let us assume that the program has determined that particles $i$ and $j$, with velocities $\boldsymbol{v}_i$, $\boldsymbol{v}_j$ and angular velocities $\boldsymbol{\omega}_i$, $\boldsymbol{\omega}_j$, collide at time $t_{ij}$. The system is advanced up to the point of contact of the two surfaces. We must now determine for each particle the (discontinuous) changes in the linear and angular momenta. (Recall that we are assuming, for simplicity, that the molecules are linear rotors, with a moment of inertia $I$, so that $\boldsymbol{J}_i = I\boldsymbol{\omega}_i$.) Denoting post-collisional values with primes, we can write these changes in terms of the collision impulse $\Delta\boldsymbol{p}$:

$$\begin{aligned} \boldsymbol{p}_i' &= \boldsymbol{p}_i + \Delta\boldsymbol{p}, \\ \boldsymbol{p}_j' &= \boldsymbol{p}_j - \Delta\boldsymbol{p}, \\ \boldsymbol{J}_i' &= \boldsymbol{J}_i + \boldsymbol{r}_{ci} \times \Delta\boldsymbol{p}, \\ \boldsymbol{J}_j' &= \boldsymbol{J}_j - \boldsymbol{r}_{cj} \times \Delta\boldsymbol{p}. \end{aligned} \tag{10}$$

$\boldsymbol{r}_{ci}$ (e.g.) is the position of the point of impact on the surface of particle $i$ measured relative to the center of this body. Notice that this formulation of the dynamics guarantees conservation of linear and angular momentum. Applying conservation of energy leads to

$$\frac{\Delta p^2}{m} + \boldsymbol{g}_{ij} \cdot \Delta\boldsymbol{p} + \frac{1}{2I}\left( |\boldsymbol{r}_{ci} \times \Delta\boldsymbol{p}|^2 + |\boldsymbol{r}_{cj} \times \Delta\boldsymbol{p}|^2 \right) = 0, \tag{11}$$

where

$$\boldsymbol{g}_{ij} = \boldsymbol{v}_{ij} + \boldsymbol{\omega}_i \times \boldsymbol{r}_{ci} - \boldsymbol{\omega}_j \times \boldsymbol{r}_{cj} \tag{12}$$

is the relative velocity of the two impacting points. Finally, since the impulse is normal to the surface (the smoothness condition), $\Delta \boldsymbol{p} = \boldsymbol{n}\Delta p$, and this gives

$$\Delta p = \frac{-\boldsymbol{g}_{ij} \cdot \boldsymbol{n}}{(1/m) + \left( |\boldsymbol{r}_{ci} \times \boldsymbol{n}|^2 + |\boldsymbol{r}_{cj} \times \boldsymbol{n}|^2 \right)/2I}. \tag{13}$$

This equation applies generally to any hard body (given $\boldsymbol{J} = I\boldsymbol{\omega}$). Computer code to illustrate the application of these equations to the simple case of hard dumb-bells appears in section 9.1.

## 5. Properties of interest

### 5.1. Introduction

In the previous sections we discussed the technical aspects of MD simulations of hard core particles. For didactical reasons we have therefore emphasized the similarities between different hard core models. Although, from a computational point of view, different hard core models (fortunately) behave rather similarly, the various models may exhibit quite distinct and interesting physical behaviour. It is, of course, this very combination of simplicity at the level of the model and complex collective behaviour that makes hard core models interesting.

It is not our intention to review here all the interesting physics that can be learned from simulations of hard core models. Rather, we shall focus on the recent results of MD simulations on assemblies of non-spherical hard core molecules, i.e. those systems that can be conveniently studied with the simulation techniques mentioned above. The models which we discuss are: infinitely thin hard rods, prolate ellipsoids, (prolate) spherocylinders and hard dumb-bells. These four model systems exhibit quite different behaviour.

In the thin hard rod system, the structural and thermodynamic properties are trivial, since there are no excluded volume effects. However, the dynamics are very interesting. The density-dependence of the transport properties is found to follow a scaling law that resembles in many ways the behaviour predicted for semi-dilute suspensions of rigid, rod-like macromolecules [48].

The structural and dynamical properties of assemblies of prolate ellipsoids are very different from those of the thin hard rod fluid. The main reason is that, in the dense ellipsoid fluid, excluded volume effects are all important. In a fluid of sufficiently anisometric ellipsoids, the anisotropy of the pair-excluded volume is the driving force behind the formation of an orientationally ordered (nematic) liquid crystalline state. The orientationally disordered (isotropic) phase and the nematic phase are separated by a weakly first-order phase transition. In the isotropic phase, the vicinity of an orientational ordering transition manifests itself in a number of interesting precursor effects, both static and dynamic. The nematic phase has static and dynamic properties that are quite different from those of the isotropic phase. Here we focus on one aspect of the nematic phase, viz. its tendency to maintain, on average, the uniform alignment of the

constituent molecules. A given deviation from uniform alignment gives rise to a restoring force, the magnitude of which is proportional to the Frank elastic constants.

The last convex hard core model that we consider is the (prolate) spherocylinder. This particle gives rise to the most complex behaviour. Spherocylinders with sufficiently large length-to-breadth ratios, can form isotropic fluids and nematic liquid crystals. But, in addition, spherocylinders may form smectic liquid crystals (i.e. orientationally ordered fluids with a 1-dimensional density modulation). Below, we shall look at the effects of these rather subtle ordering phenomena on the collective dynamical behaviour of the spherocylinder fluid.

Finally, we consider one example of a simulation on a system of non-convex hard particles, viz. hard dumb-bells. Here we focus on the similarities and differences between systems in which the distance between the constituent atoms is held fixed, and systems in which it is allowed to vary between preset limits as discussed in section 3.4.

However, before we discuss these systems in more detail, we describe in this section the various structural and dynamical properties of interest, and outline how some of them are measured in a simulation.

### 5.2. Structure

In liquid state theory there is great interest in developing a simple formalism to describe the structure of molecular fluids. Such a tool should prove invaluable in perturbation theories. In this regard hard core fluids are of special interest since it is known that the sharp repulsive interactions present in these models give rise to a structure that is similar to that of real fluids. For monatomic fluids there are now highly accurate theories for the radial distribution function $g(r)$. Indeed the hard sphere $g(r)$ can be calculated essentially exactly [7].

The corresponding theory for molecular fluids is much less well-developed. There has been progress in using fused hard sphere reference systems for small molecules [49], but much remains to be done for highly anisometric systems, and this approach is essentially restricted to the atom–atom description of liquid structure.

For molecules, the full pair distribution function depends on the molecular orientations, $\Omega_1$ and $\Omega_2$, as well as the separation of the centres of mass $r_{12}$. The usual approach is to expand this function in spherical harmonics [50]:

$$g(r_{12}, \Omega_1, \Omega_2) = 4\pi \sum_{ll'm} g_{ll'm}(r_{12}) Y_{lm}(\Omega_1) Y_{l'-m}(\Omega_2). \tag{14}$$

The orientations $\Omega_1$ and $\Omega_2$ are measured relative to the vector $\boldsymbol{r}_{12}$ in this expression. The expansion coefficients $g_{ll'm}(r_{12})$ can be calculated from simulations [51] or estimated by integral equation theories [52]. Unfortunately the series is not rapidly convergent, especially for small $r_{12}$, thereby impairing its usefulness.

For convex molecules, the following approach, at the expense of some increase in complexity, seems more promising. The idea is to base the expansion on the minimum surface–surface distance between a pair of molecules, rather than the center–center distance. For continuous potentials the equivalent procedure is to transform the coordinates from surfaces of constant $r_{12}$ to equipotential surfaces. Kabadi and Steele have examined the structure of the Gaussian overlap

fluid at constant well-depth using this technique [53]. Recently, this idea has been applied to the hard spherocylinder fluid [54].

Carrying out the coordinate transformation from center–center $(r_{12}, \Omega_1, \Omega_2)$ to surface–surface $(s_{12}, \Omega_1, \Omega_2)$ coordinates introduces a Jacobian $J(s_{12}, \Omega_1, \Omega_2)$. The appearance of this function results from the fact that surfaces of constant $s_{12}$ are non-spherical. In the new coordinate system the expectation value of some property, $X(s_{12}, \Omega_1, \Omega_2)$, is

$$\langle X \rangle = \tfrac{1}{2}\rho \int \mathrm{d}\Omega_1 \int \mathrm{d}\Omega_2 \int \mathrm{d}s_{12}\; X(s_{12}, \Omega_1, \Omega_2) G(s_{12}, \Omega_1, \Omega_2), \tag{15}$$

where $G(s_{12}, \Omega_1, \Omega_2) = g(s_{12}, \Omega_1, \Omega_2) J(s_{12}, \Omega_1, \Omega_2)$. It is convenient to expand $G$ in spherical harmonics

$$G(s_{12}, \Omega_1, \Omega_2) = 4\pi \sum_{ll'm} G_{ll'm}(s_{12}) Y_{lm}(\Omega_1) Y_{l'-m}(\Omega_2). \tag{16}$$

The coefficients $G_{ll'm}$ are easily evaluated in a simulation by averaging the appropriate product of spherical harmonics at constant $s_{12}$.

### 5.3. Transport properties

The molecular dynamics technique is, of course, essential in the calculation of the transport coefficients. For a pure fluid we are interested in the translational diffusion coefficient $D_T$, thermal conductivity $\lambda$, shear viscosity $\eta$, and bulk viscosity $\zeta$. Diffusion is a single particle property, while the remainder are collective properties. The implication of this for computer simulations is that considerably longer runs are required to calculate the collective properties to the same degree of accuracy as the diffusion coefficients [8].

There are two approaches to the calculation of the transport coefficients. Associated with each coefficient $\gamma$ is a dynamical quantity $G(t)$ [7] (see table 1). Then the corresponding transport coefficient is given either by the time integral of an autocorrelation function,

$$\gamma = \frac{k_B T}{V} \int_0^\infty \langle \dot{G}(t) \dot{G}(0) \rangle \, \mathrm{d}t, \tag{17}$$

Table 1
Dynamical variables for transport coefficients

| Dynamical variable $G$ | Transport coefficient $\gamma$ |
|---|---|
| $x_i$ | $D$ |
| $m\sum_{i=1}^{N} x_i \dot{y}_i$ | $\eta$ |
| $m\sum_{i=1}^{N} x_i \dot{x}_i - PVt$ | $\zeta + \frac{4}{3}\eta$ |
| $\sum_{i=1}^{N} x_i E_i$ | $\lambda T$ |

or by the so-called Einstein formula,

$$\gamma = \lim_{t\to\infty} \frac{k_B T}{2Vt} \langle |G(t) - G(0)|^2 \rangle = \lim_{t\to\infty} \frac{k_B T}{2V} \frac{\mathrm{d}}{\mathrm{d}t} \langle |G(t) - G(0)|^2 \rangle. \tag{18}$$

Here $k_B$ is Boltzmann's constant and $T$ the temperature. The equivalence of these expressions requires only that the autocorrelation function should decay sufficiently rapidly. Because of the impulsive nature of the forces acting between hard particles, it is more convenient to adopt eq. (18). The second form of this equation, based on the gradient with respect to time, gives the faster convergence to the result [8]. The subtraction of the $PV$ term in the expression containing the bulk viscosity (see table 1) is necessary since $\langle \dot{G} \rangle = PV$ is non-zero, so $\langle G(t) - G(0) \rangle = PVt$. The term $E_i$ in the expression for the thermal conductivity represents the single-molecule energy, i.e. the sum of kinetic and potential contributions. In the case of pairwise-additive potentials, these terms are divided equally between the participating molecules to give the single-molecule contributions.

The study of the hard sphere diffusion constant by Alder and co-workers, has greatly increased our understanding of the dynamical properties in liquids. Extensive comparison was made with the predictions of the Enskog theory. Notably, simulations led to the proposal of the hydrodynamic vortex model to explain the long-time behaviour of the velocity autocorrelation function. No similarly wide-ranging study has been undertaken for hard molecules (although comparisons of this kind have been made for rough spheres [23,26,55]). In the earliest MD simulations of non-spherical hard objects, Rebertus and Sando [45] calculated the diffusion constants for prolate spherocylinders at two liquid densities. These values are greater than the Enskog predictions.

### 5.4. Rotational dynamics

Rotational dynamics may be investigated via the orientational single-particle time correlation functions

$$C_1^s(t) = \langle P_1(\boldsymbol{u}_i(0) \cdot \boldsymbol{u}_i(t)) \rangle, \qquad C_2^s(t) = \langle P_2(\boldsymbol{u}_i(0) \cdot \boldsymbol{u}_i(t)) \rangle, \tag{19}$$

where $P_1$ and $P_2$ are first- and second-rank Legendre polynomials of the orientation vector $\boldsymbol{u}_i$ of molecule $i$. In practice, these are computed by averaging over all equivalent molecules. Rotational correlation times $\tau_1^s$ and $\tau_2^s$ are defined as time integrals of these functions. In the rotational diffusion limit, the ratio $\tau_1^s \tau_2^s$ equals 3. Also of interest are the collective orientational correlation functions,

$$\begin{aligned} C_1^c(t) &= \sum_j \langle P_1(\boldsymbol{u}_i(0) \cdot \boldsymbol{u}_j(t)) \rangle / \sum_j \langle P_1(\boldsymbol{u}_i(0) \cdot \boldsymbol{u}_j(0)) \rangle, \\ C_2^c(t) &= \sum_j \langle P_2(\boldsymbol{u}_i(0) \cdot \boldsymbol{u}_j(t)) \rangle / \sum_j \langle P_2(\boldsymbol{u}_i(0) \cdot \boldsymbol{u}_j(0)) \rangle, \end{aligned} \tag{20}$$

and their time integrals $\tau_1^c$ and $\tau_2^c$ respectively. These functions differ from those of eq. (19) by the presence of cross-correlations between different particles. In fact, for molecules with a centre

of symmetry as discussed here, the first-rank quantities $C_1^s$ and $C_1^c$ are identical, and the distinguishing superscript may be dropped. The differences between single-particle and collective rotational correlation functions become especially interesting near the isotropic–nematic (I–N) liquid crystal phase transition (see section 7).

Another probe of rotational motion is the correlation function of molecular angular velocities $\omega_i$, the time-integral of which is related to the rotational diffusion coefficient

$$D_R = \tfrac{1}{2}\int_0^\infty \langle \omega_i(t) \cdot \omega_i(0) \rangle \, \mathrm{d}t. \tag{21}$$

The correlation functions of eqs. (19) and (21) may be approximately related through the cumulant expansion formalism [56].

### 5.5. Elastic constants

The nematic liquid crystal phase is characterized by long-range ordering of the molecular orientations. In the usual uniaxial nematic phase, the distribution of molecular orientations has cylindrical symmetry. The symmetry axis of this distribution is usually referred to as the nematic *director* $\boldsymbol{n}$. In the absence of external perturbations, the direction of $\boldsymbol{n}$ will be the same throughout a macroscopic sample. Any deformation of the director pattern leads to an increase in the free-energy density of the system. The relation between the free-energy density and the distortion of the director pattern is given by [57,58]

$$\mathscr{F}(r) = \tfrac{1}{2}\left[ K_1(\nabla \cdot \boldsymbol{n})^2 + K_2(\boldsymbol{n} \cdot \nabla \times \boldsymbol{n})^2 + K_3(\boldsymbol{n} \times (\nabla \times \boldsymbol{n}))^2 \right]. \tag{22}$$

In eq. (22), $K_1$, $K_2$ and $K_3$ are the so-called Frank elastic constants for "splay", "twist" and "bend", respectively. For a direct numerical calculation of the Frank constants, eq. (22) is not particularly useful. The reason is that $\boldsymbol{n}$ itself is not a truly microscopic quantity. However, Forster [59] has given expressions which relate the Frank elastic constants to the mean-square amplitude of the long-wavelength collective orientational fluctuations. At a given wavevector $\boldsymbol{k}$ the relevant dynamical variable is the tensor $\boldsymbol{Q}(\boldsymbol{k})$

$$Q_{\alpha\beta}(\boldsymbol{k}) \equiv \frac{V}{N} \sum_{i=1}^{N} \left( \tfrac{3}{2} u_{i\alpha} u_{i\beta} - \tfrac{1}{2}\delta_{\alpha\beta} \right) \exp(\mathrm{i}\boldsymbol{k} \cdot \boldsymbol{r}_i). \tag{23}$$

If we choose our coordinate frame such that the $z$-axis coincides with the direction of $\boldsymbol{n}$ and the wavevector $k$ lies in the $xz$-plane, then we have the following simple expressions for the Frank elastic constants:

$$E_{13}(k_x^2, k_z^2) \equiv K_1 k_x^2 + K_3 k_z^2 = \frac{S^2 V k_B T}{\langle Q_{xz}(\boldsymbol{k}) Q_{xz}(-\boldsymbol{k}) \rangle} \tag{24}$$

and

$$E_{23}(k_x^2, k_z^2) \equiv K_2 k_x^2 + K_3 k_z^2 = \frac{S^2 V k_B T}{\langle Q_{yz}(\boldsymbol{k}) Q_{yz}(-\boldsymbol{k}) \rangle}. \tag{25}$$

In eqs. (24) and (25), $S$ is the nematic order parameter. It is defined as follows:

$$S = \left\langle \frac{1}{N} \sum_{i=1}^{N} P_2(\boldsymbol{u}_i \cdot \boldsymbol{n}) \right\rangle . \tag{26}$$

It should be stressed that eqs. (24) and (25) are, strictly speaking, only valid in the limit $\boldsymbol{k} \ll 2\pi/\sigma$, where $\sigma$ is a measure of the linear dimensions of the molecules under consideration. At the same time, due to the periodic boundary conditions, the components of $\boldsymbol{k}$ in the simulation periodic box axes must be equal to a multiple of $2\pi/L$, where $L$ is the box size. Combining these two conditions, we see that, if we wish to use eqs. (24) and (25) to compute the Frank constants, we need to carry out simulations on a system with linear dimensions much larger than the size of a molecule. However, there is no point in going to a larger system size if this can only be achieved at the expense of the length of the simulations (and thereby, of the statistical accuracy of the results). The linear dimensions of the systems described here (sections 7 and 8) are certainly not very large compared to the size of the individual molecules, and hence deviations from eqs. (24) and (25) should be expected. We therefore treat eqs. (24) and (25) as the leading terms in the expansion of the right hand sides in powers of $k_x^2$ and $k_z^2$. The Frank elastic constants are then obtained as the coefficients of $k_x^2$ and $k_z^2$ in a polynomial fit to the simulation data, over a range of $k$-values.

## 6. Hard lines

At first sight, infinitely thin hard rods ("hard lines") are not an interesting system to study. After all, the pair-excluded volume of hard lines vanishes and hence hard lines behave in all their static properties as an ideal gas. As a consequence there are no structural correlations of any sort in this system (i.e. $g(\boldsymbol{r}_{12}, \boldsymbol{\Omega}_1, \boldsymbol{\Omega}_2) = 1/(4\pi)^2$). However, the dynamical properties of hard lines are far from trivial, especially at high densities. Consider a system of hard lines of length $l$. It is convenient to express the number density $\rho$ of such a system as $\rho = (N/V)l^3$. For $\rho \ll 1$ the transport properties of hard lines are adequately described by kinetic theory. For other hard particle fluids there are two reasons why the low-density kinetic theory must be modified as the density is increased: the static correlations change as the density is increased, and the "molecular chaos" assumption which constitutes the basis of the conventional kinetic theory may become invalid. In the case of hard lines, there is no change in static correlations with density. Hence, any deviation from kinetic theory must be exclusively due to the failure of the molecular-chaos assumption.

In the present section we discuss the behavior of the translational and rotational diffusion constants of hard lines. The density-dependence of these two quantities provides a spectacular demonstration of the breakdown of the molecular-chaos approximation. If successive binary collisions were uncorrelated, then the translational self-diffusion constant $D_T$ would be inversely proportional to the number density $\rho$. The same would hold for the rotational diffusion constant $D_R$. However, the computer simulations [35,42] reveal a completely different density-dependence. Figure 2 shows the MD results of Magda et al. [42] for the dependence of ln $D_R$ on ln $\rho$, for

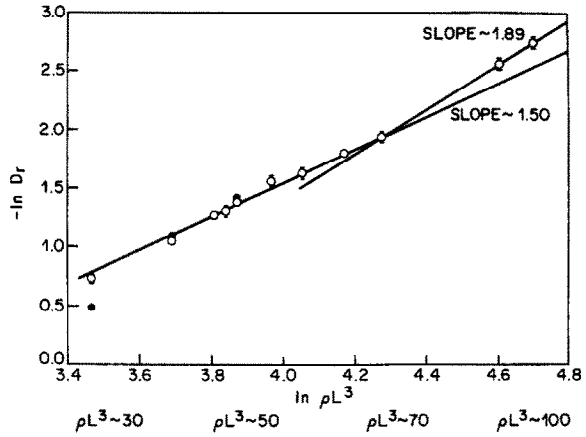


Fig. 2. Rotational diffusion constant $D_R$ as a function of density (log scales) for a system of hard lines. Open circles: data reproduced from ref. [42] by permission. Closed circles: ref. [35].

$30 < \rho < 100$. The figure clearly suggests that $D_R \propto \rho^{-s}$, with $s$ between 1.5 and 1.9, the larger slope corresponding to higher densities. Even more remarkable is the density-dependence of the translational diffusion constant $D_T$. Figure 3 shows that $D_T$ is not at all inversely proportional to $\rho$ at high densities. In fact, $D_T$ is found to *increase* with increasing $\rho$. Qualitatively, the behaviour of $D_R$ and $D_T$ can be understood, if it is assumed that, at high densities, the rotational and translational motion of thin hard rods is completely determined by the topological constraints imposed by the presence of the surrounding rods. This idea was first put forward by Doi and Edwards [48] in the context of a theoretical description of the rotational Brownian motion of rigid, rod-like polymers in a semi-dilute suspension. This theory predicts that $D_R \propto \rho^{-2}$. Frenkel and Maguire [35] have argued that a straightforward extension of the scaling theory of Doi and Edwards to a gas of smooth hard lines leads to the prediction that $D_T \propto \rho^{1/2}$. In other words, $D_T$ is predicted to *diverge* as $\rho \to \infty$. The physical reason for this rather counterintuitive behaviour is that, at high densities, the translational motion of a smooth thin

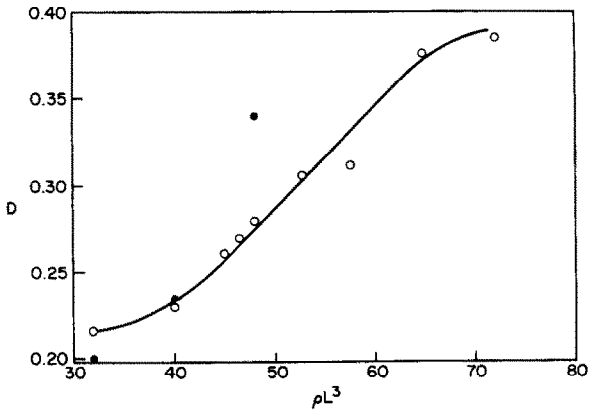


Fig. 3. Translational diffusion constant $D_T$ as a function of density for a system of hard lines. Open circles: data reproduced from ref. [42] by permission. Closed circles: ref. [35].

rod in the direction of the molecular axis, is effectively channeled by the "tube" formed by its neighbours. Due to this channeling it takes an increasingly long time interval for the molecule to transfer to the surrounding fluid that component of its linear momentum that was parallel to its axis $\boldsymbol{u}$ at the beginning of this time interval. However, although such a scaling theory explains qualitatively the trends observed in the simulations, its quantitative predictions are rather poor [42]. At present, a quantitative theoretical description of the dynamics of thin, rod-like particles at high densities is still lacking.

## 7. Hard ellipsoids

### 7.1. Introduction

Systems of molecules consisting of hard ellipsoids of revolution have been studied by MC simulation in recent years [60–64]. A major interest in this model lies in the existence of thermodynamically stable nematic liquid crystal phases for sufficiently anisometric prolate or oblate ellipsoids. We have conducted MD simulations of this system, using the retrospective collision detection method described above. We have used the program to investigate the slowing-down of molecular rotation in the isotropic liquid on approaching the nematic–isotropic transition, and the way in which this is associated with the onset of nematic long-range order [65]. The time evolution of the orientational ordering tensor has been observed as the system makes the transition from the isotropic to the nematic phase [66]. We have also reported the measurement of Frank elastic constants in the nematic phase [67]. Here we give a brief description of the computer code used in our simulation program, and follow with a summary of the simulation parameters, and an account of our results for the structure and transport coefficients in the liquid.

### 7.2. Computer code

The most expensive part of our simulation program is the detection of overlaps in a configuration obtained by advancing through a timestep using free-flight dynamics. We use the exact ellipsoid overlap criterion of Vieillard-Baron [60]. This is expressed in terms of six functions of the relative position $\boldsymbol{r}_{ij} = \boldsymbol{r}_i - \boldsymbol{r}_j$ and orientations $\boldsymbol{u}_i$, $\boldsymbol{u}_j$ of a pair of ellipsoids $i$, $j$, having semi-axes $a$ and $b$, with $e = a/b$. The functions are

$$
\begin{aligned}
g_1 &= 4 + \left(\frac{a}{b} - \frac{b}{a}\right)^2 |\boldsymbol{u}_i \times \boldsymbol{u}_j|^2 - \frac{r_{ij}^2}{b^2} + \left(\frac{1}{b^2} - \frac{1}{a^2}\right)(\boldsymbol{r}_{ij} \cdot \boldsymbol{u}_i)^2, \\
g_2 &= 4 + \left(\frac{a}{b} - \frac{b}{a}\right)^2 |\boldsymbol{u}_i \times \boldsymbol{u}_j|^2 - \frac{r_{ij}^2}{b^2} + \left(\frac{1}{b^2} - \frac{1}{a^2}\right)(\boldsymbol{r}_{ij} \cdot \boldsymbol{u}_j)^2, \\
h &= g_1 + g_2 - 2 - \frac{1}{b^2}\left(\frac{a}{b} - \frac{b}{a}\right)^2 (\boldsymbol{r}_{ij} \cdot \boldsymbol{u}_i \times \boldsymbol{u}_j)^2, \\
S_1 &= h^2 - 2g_1 g_2 - 4, \\
S_2 &= g_1^2 g_2^2 + 8g_1 g_2 - 2h(g_1^2 + g_2^2), \\
\Phi &= 4(h^2 - 3q)(q^2 + 3hw) - (9w + hq)^2,
\end{aligned}
\tag{27}
$$

where

$$q = g_1 g_2 - 4, \qquad w = 4h - g_1^2 - g_2^2. \tag{28}$$

The condition that the two ellipsoids overlap is that *all* of $(g_1, g_2, h)$ must be positive *or* at least one of $(S_1, S_2, \Phi)$ must be negative. In all practical cases (and this is checked during the running of the simulation program) the function $\Phi$ changes sign on contact, and so this function alone can play the role of the overlap function $f_{ij}$ in eq. (9). An expression for the time derivative of $\Phi$ is required, in order to locate the root of this equation by the Newton–Raphson method, and this is readily obtained given the velocities and angular velocities of the molecules. Perram and Wertheim [62,64] have devised another exact overlap criterion, involving the numerical maximization of a function $f_{ij}^{\mathrm{PW}}(\lambda)$ of molecular positions and orientations with respect to a parameter $\lambda$, which may take values between 0 and 1. The function $\max_{0 \le \lambda \le 1} f_{ij}^{\mathrm{PW}}(\lambda)$ is equal to unity at contact; lower values indicate overlap while higher values correspond to non-overlapping ellipsoids. We have checked the equivalence of this prescription with that of Vieillard-Baron for every collision detected in our simulations. We also adopt the suggestion of Perram and Wertheim, that the particular choice $\lambda = \frac{1}{2}$ can be used to rapidly eliminate the possibility of overlap. The function $f_{ij}^{\mathrm{PW}}(\lambda = \frac{1}{2})$ is relatively economical to evaluate:

$$f_{ij}^{\mathrm{PW}}(\lambda = \tfrac{1}{2}) = \frac{r_{ij}^2}{4b^2} + \frac{x(1-x)\left((\boldsymbol{r}_{ij}\cdot\boldsymbol{u}_i)^2 + (\boldsymbol{r}_{ij}\cdot\boldsymbol{u}_j)^2\right) + 2x^2(\boldsymbol{u}_i\cdot\boldsymbol{u}_j)(\boldsymbol{r}_{ij}\cdot\boldsymbol{u}_i)(\boldsymbol{r}_{ij}\cdot\boldsymbol{u}_j)}{4Db^2}, \tag{29}$$

where

$$x = (1 - e^2)/2, \qquad D = (1 - x^2) - x^2(\boldsymbol{u}_i\cdot\boldsymbol{u}_j)^2. \tag{30}$$

If $f_{ij}^{\mathrm{PW}}(\lambda = \frac{1}{2}) > 1$, then ellipsoids $i$ and $j$ cannot overlap. We refer to this as the "quick Perram–Wertheim" test. It can be applied after an initial examination to see if the ellipsoid centre–centre distance is greater than the diameter of the circumscribing sphere $\sigma \equiv 2\max(a, b)$.

Several of the terms appearing in eqs. (27)–(30) can be evaluated, together with other useful constants, at the start of the program.

```
C**PARAMETERS FOR CIRCUMSCRIBING SPHERE TEST**

      SIGMA   = 2.0*MAX(A,B)
      SIGSQ   = SIGMA**2

C**PARAMETERS FOR VIEILLARD-BARON TEST**

      ESQ     = E**2
      ESQ1    = 1.0 - ESQ
      ASQ     = A**2
      BSQ     = B**2
      OASQ    = 1.0/ASQ
```

```
      OBSQ   = 1.0/BSQ
      ABBA2  = (E - 1.0/E)**2
      OB2A2  = OBSQ - OASQ
      OB2ABA = OBSQ*ABBA2

C**PARAMETERS FOR QUICK PERRAM-WERTHEIM TEST**

      X      = 0.5*ESQ1
      X1     = 1.0 - X
      XSQ    = X**2
      X1SQ   = X1**2
      ALPHA  = X*X1
      OBSQ4  = 0.25*OBSQ
```

In a routine to detect overlaps between specific ellipsoids, the circumscribing sphere, quick Perram–Wertheim, and exact Vieillard-Baron tests are applied in succession. At each stage, assuming that the processing is on a scalar computer or that scalar mode is in operation, there is an advantage in dropping out of the test sequence as early as possible. In the following piece of code, taken from an overlap detection subroutine, we indicate this by an immediate RETURN should the possibility of overlap be eliminated. In this example, we begin with the calculation of minimum image vectors in truncated octahedral periodic boundaries, and take the containing cube to be of unit side. The variable R75 stores the value $\frac{4}{3}$.

```
      OVRLAP = .FALSE.

      RXIJ   = RXI - RXJ
      RYIJ   = RYI - RYJ
      RZIJ   = RZI - RZJ

C**MINIMUM IMAGE CONVENTION, TO BOUNDARIES**

      RXIJ   = RXIJ - ANINT(RXIJ)
      RYIJ   = RYIJ - ANINT(RYIJ)
      RZIJ   = RZIJ - ANINT(RZIJ)
      CORR   = 0.5*AINT(R75*(ABS(RXIJ) +
     :                ABS(RYIJ) +
     :                ABS(RZIJ)))
      RXIJ   = RXIJ - SIGN(CORR,RXIJ)
      RYIJ   = RYIJ - SIGN(CORR,RYIJ)
      RZIJ   = RZIJ - SIGN(CORR,RZIJ)

C**CIRCUMSCRIBING SPHERE TEST**

      RIJSQ = RXIJ**2 + RYIJ**2 + RZIJ**2

      IF (RIJSQ.GT.SIGSQ) RETURN
```

```
C**QUICK PERRAM-WERTHEIM TEST**
      RUI    = RXIJ*UXI + RYIJ*UYI + RZIJ*UZI
      RUJ    = RXIJ*UXJ + RYIJ*UYJ + RZIJ*UZJ
      RUISQ  = RUI**2
      RUJSQ  = RUJ**2
      UIUJ   = UXI*UXJ + UYI*UYJ + UZI*UZJ
      GAMMA  = XSQ*UIUJ
      DENOM  = X1SQ - GAMMA*UIUJ
      F      = OBSQ4*(RIJSQ +
     :       (ALPHA*(RUISQ + RUJSQ) +
     :       2.0*GAMMA*RUI*RUJ)/DENOM)
      IF (F.GT.1.0) RETURN
C**VIEILLARD-BARON TESTS**
      UVECX  = UYI*UZJ - UZI*UYJ
      UVECY  = UZI*UXJ - UXI*UZJ
      UVECZ  = UXI*UYI - UYI*UXJ
      UVECSQ = 1.0 - UIUJ**2
      RUIUJ  = RXIJ*UVECX + RYIJ*UVECY + RZIJ*UVECZ
      G      = 4.0 + ABBA2*UVECSQ - RIJSQ*OBSQ
      G1     = G + OB2A2*RUISQ
      G2     = G + OB2A2*RUJSQ
      H      = G1 + G2 - 2.0 - OB2ABA*RUIUJ**2
      SMALL  = MIN(G1,G2,H)
      IF (SMALL.GT.0.0) GOTO 100
      G1G2   = G1*G2
      HSQ    = H**2
      S1     = HSQ - 2.0*G1G2 - 4.0
      IF (S1.LT.0.0) GOTO 100
      GSQSUM= G1**2 + G2**2
      S2     = G1G2*(8.0 + G1G2) - 2.0*H*GSQSUM
      IF (S2.LT.0.0) GOTO 100
      Q      = G1G2 - 4.0
      W      = 4.0*H - GSQSUM
      PHI    = 4.0*(HSQ - 3.0*Q)
     :       *(Q**2 + 3.0*W*H)
     :       - (9.0*W + H*Q)**2
      IF (PHI.LT.0.0) GOTO 100
      RETURN
C**OVERLAP DETECTED**
100   OVRLAP = .TRUE.
      RETURN
```

The initial part of the complete search over pairs, i.e. the application of the sphere and quick Perram-Wertheim tests, can be vectorized. In vector mode, we find that it does not save time to

do a preliminary circumscribing sphere test. We do, however, find it economical to employ a Verlet neighbour list, as mentioned in section 4.3. We illustrate this with the following FORTRAN 200 code as written for a CYBER 205 computer; it would be simple to convert this for other machines, but it should be noted that we make use of supplied routines to "gather" (Q8VGATHR) and "compress" (Q8VCMPRS) particle index lists. The complete set of molecular positions is stored in RX(1;N), RY(1;N), RZ(1;N) and all the orientation vectors are in UX(1;N), UY(1;N), UZ(1;N). The neighbour list itself is stored in two arrays LISTI and LISTJ. Corresponding elements of these arrays contain the indices of molecules which are neighbours. Suppose that there are NLIST neighbour pairs in this list. For simplicity, we illustrate the case where all NLIST pairs are processed at once. In a practical application, since the list can be very long, we would break this operation up and process pairs a thousand (say) at a time. Symbolic names representing FORTRAN 200 vector descriptors are distinguished by a final letter D; all of these represent vectors of length NLIST, so a typical assignment statement would be ASSIGN LISTID, LISTI(1;NLIST). We omit these ASSIGN statements for clarity and brevity. A bit vector, represented by a descriptor BITD, is set to hold TRUE values wherever a pair is found to satisfy the quick Perram–Wertheim criterion for possible overlap. The function Q8SCNT returns the number of such TRUE values. The final result of this piece of code is a shorter list, stored in NEWI(1;NNEW), NEWJ(1;NNEW), containing indices of pairs of molecules which pass the quick Perram–Wertheim test. The scalar variables appearing below have the same significance as in the previous example.

```
C**GATHER MOLECULAR ORIENTATIONS FOR PAIRS ON THE LIST**

      UXID    = Q8VGATHR(UX(1;N),LISTID,UXID)
      UYID    = Q8VGATHR(UY(1;N),LISTID;UYID)
      UZID    = Q8VGATHR(UZ(1;N),LISTID;UZID)
      UXJD    = Q8VGATHR(UX(1;N),LISTJD;UXJD)
      UYJD    = Q8VGATHR(UY(1;N),LISTJD;UYJD)
      UZJD    = Q8VGATHR(UZ(1;N),LISTJD;UZJD)

C**GATHER MOLECULAR SEPARATIONS FOR PAIRS ON THE LIST**

      RXIJD   = Q8VGATHR(RX(1;N),LISTID;RXIJD)
      RYIJD   = Q8VGATHR(RY(1;N),LISTID;RYIJD)
      RZIJD   = Q8VGATHR(RZ(1;N),LISTID;RZIJD)
      RXIJD   = RXIJD - Q8VGATHR(RX(1;N),LISTJD;TMPXD)
      RYIJD   = RYIJD - Q8VGATHR(RY(1;N),LISTJD;TMPYD)
      RZIJD   = RZIJD - Q8VGATHR(RZ(1;N),LISTJD;TMPZD)

C**MINIMUM IMAGE CONVENTION, TO BOUNDARIES**

      RXIJD   = RXIJD - VANINT(RXIJD;TMPXD)
      RYIJD   = RYIJD - VANINT(RYIJD;TMPYD)
      RZIJD   = RZIJD - VANINT(RZIJD;TMPZD)
```

```
      CORRD  = VAINT(R75*(VABS(RXIJD;TMPXD) +
     :VABS(RYIJD;TMPYD) +
     :VABS(RZIJD;TMPZD));CORRD)
      CORRD  = 0.5*CORRD
      RXIJD  = RXIJD - VSIGN(CORRD,RXIJD;TMPXD)
      RYIJD  = RYIJD - VSIGN(CORRD,RYIJD;TMPYD)
      RZIJD  = RZIJD - VSIGN(CORRD,RZIJD;TMPZD)

C**QUICK PERRAM-WERTHEIM TEST**

      RSQD   = RXIJD**2 + RYIJD**2 + RZIJD**2
      RUID   = RXIJD*UXID + RYIJD*UYID + RZIJD*UZID
      RUJD   = RXIJD*UXJD + RYIJD*UYJD + RZIJD*UZJD
      UIJD   = UXID*UXJD + UYID*UYJD + UZID*UZJD
      GAMMAD= XSQ*UIJD
      DENOMD= X1SQ - GAMMAD*UIJD
      FD     = ((RUID**2 + RUJD**2)*ALPHA
     :+ GAMMAD*(2.0*RUID*RUJD))/DENOMD
      FD     = OBSQ4*(RSQD + FD)
      BITD   = FD.LE.1.0
      NNEW   = Q8SCNT(BITD)
      IF (NNEW.LE.0) RETURN
      NEWI(1;NNEW) = Q8VCMPRS(LISTID,BITD;NNEW)
      NEWJ(1;NNEW) = Q8VCMPRS(LISTJD,BITD;NNEW)
      RETURN
```

The pairs appearing in the new list are then processed in scalar mode, and the exact Vieillard-Baron overlap criterion is applied to each of them, just as in the first example.

The neighbour list itself is generated, at intervals, by a routine almost identical to the one above. There are three points of difference. Firstly, instead of starting with an existing list in LISTI, LISTJ, the input to this latter routine is the complete set of distinct $(i, j)$ pair indices in the system. Again, in practice, this list is so long that it must be broken down into manageable chunks. Secondly, the output from this routine is not NEWI, NEWJ but LISTI, LISTJ. Finally, the function used to generate the list is actually based on the (approximate) "quick Perram–Wertheim" criterion for overlap of two ellipsoids larger than, and completely containing, the actual molecules. This corresponds to replacing the condition $f_{ij}^{\mathrm{PW}}\ (\lambda = \frac{1}{2}) \leq 1$ (which admits the possibility of overlap) by $f_{ij}^{\mathrm{PW}}\ (\lambda = \frac{1}{2}) \leq f_{\mathrm{list}}$ where $f_{\mathrm{list}}$ is some user-specified value (greater than 1). (Note how $f_{ij}^{\mathrm{PW}}\ (\lambda = \frac{1}{2})$ in eq. (29) scales with $r_{ij}^2/b^2$). In the above code, FD.LE.1.0 is replaced by FD.LE.FLIST.

Periodic regeneration of the list is accompanied by checks to guard against molecules crossing the "safety skin" in between updates. Just before updating the list, the program calculates the minimum value of $f_{ij}^{\mathrm{PW}}\ (\lambda = \frac{1}{2})$ for pairs *not* on the list. Values close to 1 indicate that significant penetration of the safety skin is occurring, and the program lowers the interval between updates accordingly. (Values less than 1 indicate a possible overlap of molecules not on the neighbour

list, and lead to an immediate check using the exact Vieillard-Baron criterion: should such an overlap ever be detected, the program would terminate immediately with an error message).

### 7.3. Simulation parameters

We have investigated prolate ellipsoids, with the following axial ratios $e = a/b = 2, 3, 5, 10$, and oblate ellipsoids with $e = 1/3$, $a$ and $b$ being the semi-axis lengths. Only results for $e = 2, 3, 1/3$ will be presented here. In the MD simulations, the molecules are taken to be of unit mass $m$, but it is also necessary to decide upon a mass distribution, and hence an inertia tensor. As discussed in section 4.1 we take our ellipsoids to be smooth, so collisions cannot alter the angular momentum about the symmetry axis. This leads us to set that component to zero along with the corresponding component of the inertia tensor, and to treat the molecules throughout as linear rotors. The other two inertia components, corresponding to rotation about axes perpendicular to the symmetry line, are equal in magnitude. In most of our work so far we have made this value consistent with a uniform distribution of mass throughout the body of the ellipsoid:

$$I/m = (a^2 + b^2)/5. \tag{31}$$

We have also tested an interesting alternative, sensible only for prolate ellipsoids, in which the mass is taken to be concentrated at the foci:

$$I/m = a^2 - b^2. \tag{32}$$

This results in an increase in the moment of inertia over that given in eq. (31) by a factor of 3 for $e = 2$ and by a factor of 4 for $e = 3$, rising to a factor of 5 in the limit of extreme elongation $e \to \infty$. The pointwise distribution is probably more appropriate if the ellipsoids are to be compared with small, diatomic, molecules, while the uniform mass density is a better model of large molecules or colloidal particles. Of course, this choice only affects dynamical, not static or structural, properties.

The results reported here are for system sizes of $N = 144$ molecules, in a cuboidal simulation box, and $N = 125$, 216, 512 molecules in truncated octahedral boundaries. For these systems, with axial ratios of 2–3, at liquid densities around 0.7–0.8 of the close-packed solid density, the program generates about one million collisions per hour of CYBER 205 cpu time. To obtain accurate collective transport properties, especially for the higher densities, we undertook rather long runs: typically several million collisions. The run parameters appear in table 2.

### 7.4. Diffusion coefficients

In fig. 4 we present results for the diffusion coefficient for ellipsoids of elongation $e = 2, 3, 1/3$ at various densities. As in the case of hard spheres [9] we find the translational diffusion coefficient to be quite sensitive to system size. Here we present results for the case $N = 125$ only; we have not attempted to extrapolate to the thermodynamic limit. In the isotropic phase log $D_T$ varies roughly linearly with density. In the nematic liquid crystal phase there are two diffusion coefficients, $D_T^{\parallel}$ and $D_T^{\perp}$, respectively parallel and perpendicular to the director. For the prolate

Table 2
Run parameters for hard ellipsoids

| Elongation $e = a/b$ | Density $\rho/\rho_{cp}$ | System size * $N$ | Run length ** | | Collisions $N_c/10^6$ |
|---|---|---|---|---|---|
| | | | $t_{run}$ | $t_{run}/t_c$ | |
| 2 | 0.30 | 125 | 1700 | 14000 | 0.870 |
| 2 | 0.40 | 125 | 1125 | 16000 | 1.002 |
| 2 | 0.50 | 125 | 600 | 14400 | 0.899 |
| 2 | 0.50 | 144 | 50 | 1200 | 0.087 |
| 2 | 0.60 | 125 | 320 | 12900 | 0.804 |
| 2 | 0.60 | 144 | 60 | 2400 | 0.175 |
| 2 | 0.70 | 125 | 175 | 12100 | 0.759 |
| 2 | 0.70 | 144 | 80 | 5600 | 0.400 |
| 2 | 0.80 | 125 | 110 | 13900 | 0.871 |
| 2 | 0.80 | 144 | 150 | 19100 | 1.374 |
| 3 | 0.10 | 125 | 5500 | 13200 | 0.822 |
| 3 | 0.30 | 125 | 1080 | 12700 | 0.796 |
| 3 | 0.40 | 125 | 600 | 12400 | 0.775 |
| 3 | 0.50 | 125 | 350 | 12200 | 0.763 |
| 3 | 0.60 | 125 | 240 | 14000 | 0.877 |
| 3 | 0.60 | 512 | 70 | 4100 | 1.050 |
| 3 | 0.70 | 144 | 450 | 45300 | 3.260 |
| 3 | 0.75 | 125 | 300 | 35900 | 2.240 |
| 3 | 0.75 | 144 | 600 | 70800 | 5.100 |
| 3 | 0.75 | 216 | 675 | 26800 | 2.890 |
| 5 | 0.20 | 125 | 1200 | 12000 | 0.750 |
| 5 | 0.30 | 125 | 640 | 12400 | 0.778 |
| 5 | 0.40 | 125 | 340 | 11500 | 0.719 |
| 1/3 | 0.40 | 125 | 600 | 13200 | 0.826 |
| 1/3 | 0.50 | 125 | 340 | 12900 | 0.805 |
| 1/3 | 0.60 | 125 | 200 | 12900 | 0.809 |
| 1/3 | 0.75 | 125 | 300 | 40900 | 2.554 |

* $N = 144$ corresponds to cuboidal periodic boundary conditions, other system sizes to truncated octahedral boundaries.

** We give the simulation run length both in simulation units ($k_B T = 1$, $m = 1$, $8ab^2 = 1$) and as a multiple of the mean time between collisions per particle, $t_c$.

ellipsoid case, we see enhanced diffusion along the director, and inhibited diffusion perpendicular to it, compared with the value obtained by extrapolating the isotropic phase results. For oblate ellipsoids, diffusion along the director is significantly inhibited. None of these gross features is unexpected, bearing in mind the molecular shapes. However, surprising evidence of collective behaviour in the isotropic liquid does emerge from a comparison of $D_T$ with the Enskog theory prediction $D_T^E$ [68]. At medium density, a significant enhancement of the translational diffusion coefficient, much more than observed for hard spheres, can be seen (fig. 5). The effect increases with molecular elongation, and is also present, although rather less dramatic, for oblate ellipsoids. Nonetheless, Enskog theory is very satisfactory for the rotational

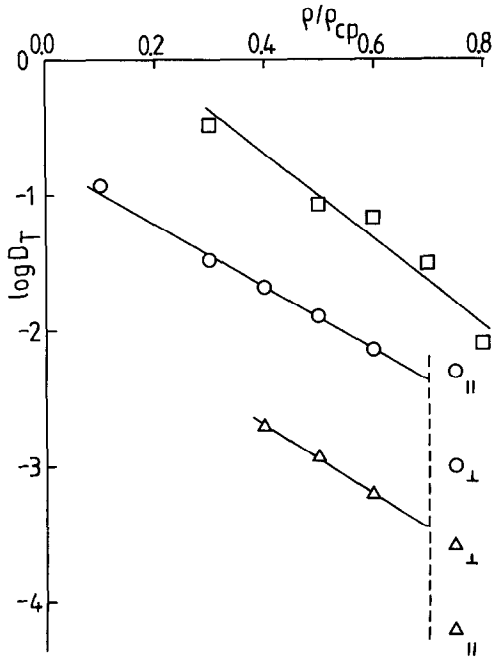


Fig. 4. Translational diffusion coefficients $D_T$ (log scale) as function of density $\rho/\rho_{cp}$, for hard ellipsoids. The systems size is $N=125$. Squares: $e=2$. Circles: $e=3$ displaced down by one unit for clarity. Triangles: $e=1/3$ displaced down by two units for clarity. In the latter two cases, the nematic phase is stable to the right of the dashed line, and two distinct diffusion coefficients exist, respectively parallel (||) and perpendicular ( $\perp$ ) to the director. The solid lines are to guide the eye.

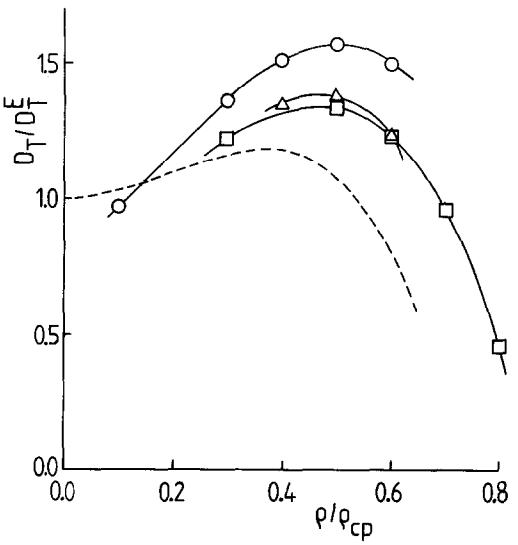


Fig. 5. Translational diffusion coefficients relative to the Enskog prediction $D_T/D_T^E$ as a function of density $\rho/\rho_{cp}$, for hard ellipsoids. The system size is $N=125$. Squares: $e=2$. Circles: $e=3$. Triangles: $e=1/3$. The solid lines are to guide the eye. For comparison, we also show the hard sphere results (dashed line) for $N=108$ (see ref. [8]).

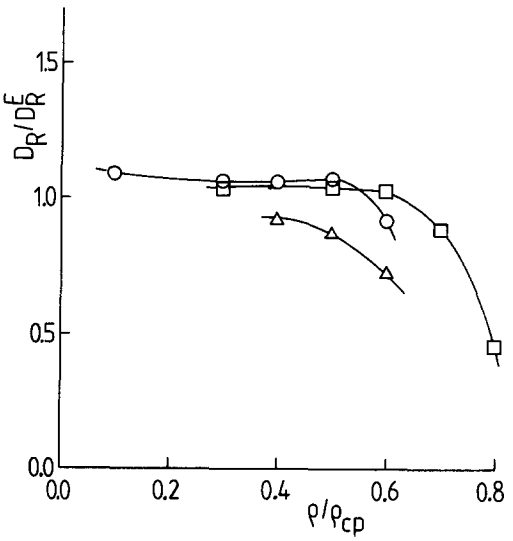


Fig. 6. Rotational diffusion coefficients relative to the Enskog prediction $D_R/D_R^E$ as a function of density $\rho/\rho_{cp}$, for hard ellipsoids. The system size is $N=125$. Squares: $e=2$. Circles: $e=3$. Triangles: $e=1/3$. The solid lines are to guide the eye.

diffusion coefficient $D_R$ at these same densities, irrespective of elongation (fig. 6). We also find the rotational diffusion coefficients to be insensitive to system size. Currently, we do not have a quantitative explanation of these effects. Presumably, as in the case of hard spheres, the enhancement of $D_T/D_T^E$ can be associated with coupling to the hydrodynamic vortex mode, although for the small systems studied here, we can see no *direct* evidence of long-time tails. The system-size dependence of $D_T$ can be attributed to the effect of periodic boundary conditions on the long-time hydrodynamics [69]. At high density, caging results in a rapid decrease of both $D_T/D_T^E$ and $D_R/D_R^E$.

### 7.5. Structure

We have already discussed the calculation of structural quantities $G_{ll'm}(s)$ in terms of a minimum surface–surface distance $s$ (section 5.2). To evaluate these quantities we require an efficient algorithm for evaluating $s$. For ellipsoids, M. Wertheim and J. Talbot have developed such a prescription [70], and we have implemented it in our computer programs.

In fig. 7 we present some preliminary results of this expansion applied to the hard ellipsoid fluid. We show the expansion coefficients for the state point $e=2$, $\rho/\rho_{cp}=0.6$. Our expectations are borne out here and for the other cases so far examined: the series of eq. (16) is rapidly convergent with only the first few terms differing significantly from zero even at short distance. Of particular interest is the striking agreement between $G_{000}(s)$ and a hard sphere $G(s)$ (i.e. $g(r)$ with $r=s+\sigma$, where $\sigma$ is the hard sphere diameter) calculated at the same packing fraction and particle volume. The agreement extends through the first coordination shell, and is especially impressive at low densities where only close to contact is there a significant difference (the ellipsoid function has a higher value). At separations beyond the first coordination shell,

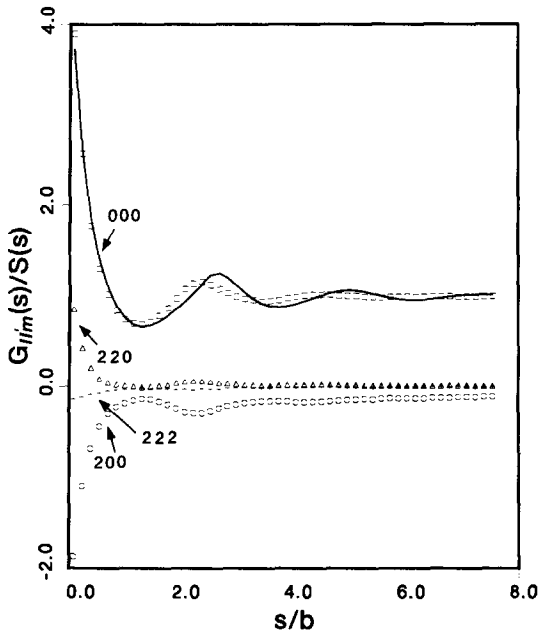


Fig. 7. Spherical harmonic expansion coefficients as functions of the surface-to-surface distance $s$ for prolate hard ellipsoids with axial ratio $e = a/b = 2$ at a density $\rho/\rho_{cp} = 0.6$ ($N = 512$). The solid line represents the radial distribution function of a hard sphere fluid at the same density and where each sphere has the same volume as an ellipsoid. $S(s)$ is the surface-area function (see ref. [71] for further details).

however, the hard ellipsoid and "equivalent" hard sphere functions become out of phase, as would be expected. A complete discussion of these results will appear in a future article [71].

### 7.6. Pretransitional dynamics

In real liquid-crystal forming fluids, strong pretransitional fluctuations may be observed when the I–N (isotropic to nematic) transition is approached from the isotropic side. In particular, there is a pronounced increase in the amplitude of collective orientational fluctuations, which results, among other things, in enhanced depolarized light scattering. A measure for the amplitude of collective orientational fluctuations with wavevector $\boldsymbol{k}$ is the tensor $\boldsymbol{Q}(\boldsymbol{k})$ defined by eq. (23). The intensity of the depolarized light scattering spectrum in the isotropic phase $I_d$ is, to a first approximation, proportional to the average trace of the square of $\boldsymbol{Q}(\boldsymbol{k} = \boldsymbol{0})$:

$$I_d \propto \langle Q_{\alpha\beta} Q_{\beta\alpha} \rangle \tag{33}$$

It is easy to show that $I_d$ in eq. (33) is a measure for the degree of correlation between the orientation of different molecules. In fact, $\langle Q_{\alpha\beta} Q_{\beta\alpha} \rangle \; N/V^2$ can be rewritten as $(1 + g_2)$, where $g_2$ is the static orientational correlation factor, defined as

$$g_2 = \sum_{j \neq i} P_2(\boldsymbol{u}_i \cdot \boldsymbol{u}_j). \tag{34}$$

The proximity of the isotropic–nematic transition influences not just the static orientational properties of the fluid but also the rotational dynamics. In particular, the relaxation time $\tau_2^c$ of the collective orientational fluctuations (see section 5.4) appears to diverge as the I–N transition is approached. The relation between this divergence of $\tau_2^c$ and the behaviour of $g_2$ is of particular interest. Using Mori theory, Keyes and Kivelson [72] derived the following expression relating $g_2$ to $\tau_2^c$:

$$\tau_2^s/\tau_2^c = (1 + j_2)/(1 + g_2). \tag{35}$$

In eq. (35), $\tau_2^s$ is the single-particle orientational correlation time and $j_2$ is the so-called dynamic orientational correlation factor. The latter quantity can be expressed in terms of memory functions, but has no simple physical interpretation. A direct experimental determination of $(1 + g_2)$ and $\tau_2^s/\tau_2^c$ is complicated by the fact that in real liquids part of the depolarized light scattering intensity is interaction induced. It is not trivial to extract the purely orientational contribution to the scattering intensity from the total spectral intensity [73]. As a consequence, there is a scarcity of reliable data from which $j_2$ can be determined. The available information [74,75,76] suggests that $j_2$ is small compared to 1, and it is common practice among experimentalists to assume that $j_2 = 0$. Using kinetic theory, Evans and coworkers [17,77,78] have derived explicit expressions for $j_2$ for hard ellipsoids and hard spherocylinders. In the low-density limit (or, more precisely, in the limit that the radial distribution function at contact becomes isotropic), Evans et al. gave the following expression for ellipsoids:

$$1 + j_2 \approx \frac{1}{1 + (2/5)\exp(-\epsilon/10)}, \tag{36}$$

where $\epsilon = e^2 - 1$. Note that $j_2$ is predicted to be small and negative. No predictions exist for the behaviour of $j_2$ at higher densities, in particular, in the vicinity of a transition to the nematic state.

Numerical simulation offers a unique possibility to study the static and dynamic precursor effects to the I–N transition in simple model systems [65]. In order to distinguish possible pretransitional effects for the "normal" density dependence of collective orientational fluctuations, we studied the rotational dynamics of a fluid of hard ellipsoids with $e = a/b = 3$, a system that forms a stable nematic phase, and also $e = 2$, which does not. Figure 8 shows typical examples of the single-particle orientational correlation functions $C_1^s(t)$ and $C_2^s(t)$ (see section 5.4). We find that the rotational diffusion relation $\tau_1^s/\tau_2^s \approx 3$ is satisfied at not too low densities. Both single particle relaxation times grow as the density is increased. This is simply a consequence of the rapid increase of the viscosity as the density of the fluid is raised, and the effect is observed for both shapes of ellipsoids. The density dependence of the collective orientational correlation function, $C_2^c(t)$ is more interesting. At low densities, the decay of $C_2^c(t)$ closely follows that of $C_2^s(t)$, as can be seen from fig. 8. However, as the density is increased, the decay of the collective orientational correlation function becomes much slower than that of the corresponding single particle one. This indicates that cooperative effects in the rotational dynamics become important at high densities. This is true both for the $e = 2$ and for the $e = 3$ case. Figure 9 shows the density dependence of the ratio $\tau_2^c/\tau_2^s$ for both shapes of ellipsoids. In

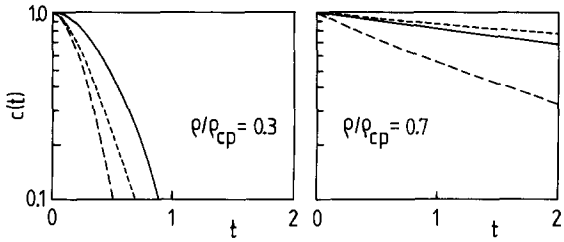


Fig. 8. Orientational correlation functions $C_1(t)$ (solid line), $C_2^s(t)$ (long dashes) and $C_2^c(t)$ (short dashes) for hard ellipsoids of axial ratio $e = 3$ at two different densities.

the same figure we have also plotted the corresponding values of $(1 + g_2)$. The difference in the behaviour of the $e = 3$ and $e = 2$ ellipsoids is immediately apparent. Although for $e = 2$ there is some evidence for cooperative behaviour, there is no sign of diverging fluctuations or critical slowing down, even at the freezing density (at 84% of close packing). In contrast, the results for $e = 3$ clearly show pretransitional effects. Both $\tau_2^c/\tau_2^s$ and $(1 + g_2)$ appear to diverge as the transition to the nematic phase is approached. If the dynamic orientational correlation factor $j_2 = 0$, then the data points for $\tau_2^c/\tau_2^s$ and $(1 + g_2)$ should superimpose. On this point the present simulations appear inconclusive, due to poor statistics. Clearly, it is not meaningful to extract estimates for $j_2$ from the individual data points. We therefore attempted to estimate $j_2$ in the following way. We assumed $(\tau_2^s/\tau_2^c)(1 + g_2)(= 1 + j_2)$ was independent of density, and carried out a linear least squares fit to the data points. The results of these fits are indicated as drawn lines in fig. 9. We see that for both shapes the estimate for $(1 + j_2)$ is less than 1. For the $a/b = 3$ case, where we have the largest number of data points, the fit suggests that $j_2$ is small and negative (typically $-0.08 \pm 0.05$). For the $a/b = 2$ ellipsoids the estimated value of $j_2$ is slightly more negative ($-0.26 \pm 0.16$), but the estimated error is also larger. Although the estimated errors in $j_2$ are large, we note that the simulation data seem to follow the trend predicted by kinetic theory, namely that $1 + j_2$ is less than 1, and approaches 1 as the molecules become more elongated. In fact, the present data do not differ significantly from the low-density kinetic theory

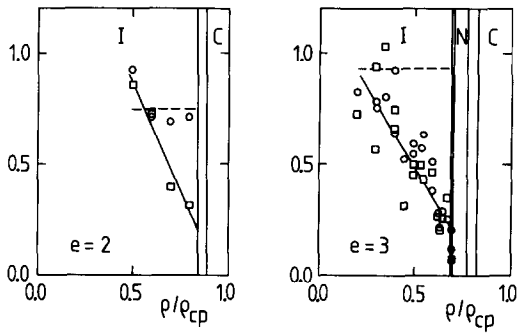


Fig. 9. Density dependence of the ratio $\tau_2^c/\tau_2^s$ (squares) for prolate ellipsoids with $e = a/b = 2$, 3. We also show $(1 + g_2)$ (circles). The estimated values of $1 + j_2$ are shown as horizontal dashed lines (see text). The isotropic liquid (I), nematic liquid crystal (N) and crystalline (C) phases are indicated, with coexistence regions delimited by vertical lines.

predictions, eq. (36): $j_2 = -0.15$ for $e = 3$, and $j_2 = -0.23$ for $e = 2$. Incidentally, the light-scattering experiments of Gierke and Flygare on a real nematogen led to comparable estimates for $j_2$ ($j_2 = -0.3 \pm 0.3$ for MBBA). However, in view of the large statistical error in both experiment and simulation, one should not attach too much significance to this apparent agreement.

### 7.7. Elastic constants

In the previous section we discussed the pretransitional behaviour of a fluid of hard ellipsoids as the isotropic–nematic transition is approached from the isotropic side. The present section describes a study of the properties of the nematic phase itself. The simulations described here (see also ref. [67]) were performed on systems of $N = 125$, 144, 216 ellipsoids with $e = 3$. Thus, although some checks of system-size dependence have begun, these systems are still quite small and the caveats of section 5.5 should be borne in mind. In all cases the density corresponded to 75% of regular close packing, a state point well within the nematic region.

To calculate the elastic constants, we made use of eqs. (24) and (25); the calculation involves a two-variable fit to a $k$-dependent quantity calculated in the simulation. In the original work [67], using cuboidal periodic boundaries, the director was approximately aligned with one of the box axes throughout the simulations. Adopting the assumption of perfect alignment made it easy to accumulate data for fixed values of $k_x$, $k_z$, components of $\boldsymbol{k}$ consistent with the box periodicity. (Recall that we take the director to be in the $z$-direction.) Fits were carried out in the two orthogonal directions $x$ and $z$. This situation did not hold for the simulations in truncated octahedral simulation boxes: the director was found not to be aligned with a box axis, and to exhibit a slow (and slight) variation with time. We are in the process of testing different approaches to fitting the functions of eqs. (24) and (25) while taking account of these features. Here we outline one such approach.

Eqs. (24) and (25) are re-written in terms of $k^2 = k_x^2 + k_z^2$ and $\Delta = k_x^2 - k_z^2$. Data is accumulated as a set of short-time averages, $E_{13}(k^2, \Delta)$, $E_{23}(k^2, \Delta)$, for a large number of values of $\Delta$, determined by the short-time average director orientation in the box, along lines of constant $k^2$. For each such value of $k^2$, least-squares polynomial fits to the data as functions of $\Delta$ are carried out; interpolated values and derivatives with respect to $\Delta$ are obtained at the origin. According to eq. (24), for the 13 symmetry case, these should be given by:

$$E_{13}(k^2, \Delta = 0) = \tfrac{1}{2}(K_1 + K_3)k^2, \qquad D_{13}(k^2, \Delta = 0) = \tfrac{1}{2}(K_1 - K_3), \tag{37}$$

where $D_{13} \equiv \partial E_{13}/\partial \Delta$. Similarly

$$E_{23}(k^2, \Delta = 0) = \tfrac{1}{2}(K_2 + K_3)k^2, \qquad D_{23}(k^2, \Delta = 0) = \tfrac{1}{2}(K_2 - K_3), \tag{38}$$

with $D_{23} \equiv \partial E_{23}/\partial \Delta$. These expressions will be expected to hold in the limit $k^2 \to 0$.

In figs. 10 and 11 we show the above functions of $k^2$ as determined from simulations of the three different system sizes. These figures are presented to demonstrate a measure of consistency between the results obtained from different sizes and shapes of the periodic box. Least squares fits to $E_{13}$, $E_{23}$, giving the initial gradients, and to $D_{13}$, $D_{23}$, yielding the intercepts, should

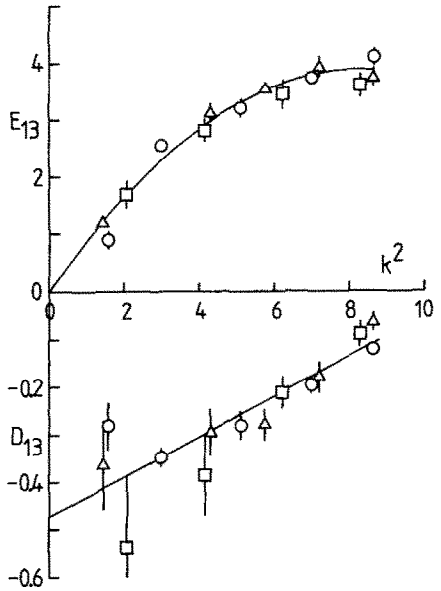


Fig. 10. The functions $E_{13}(k^2, \Delta = 0)$ and $D_{13}(k^2, \Delta = 0)$ for prolate hard ellipsoids with $e = 3$, $\rho/\rho_{cp} = 0.75$ (nematic). Squares: $N = 125$, truncated octahedral boundaries. Circles: $N = 144$, cuboidal boundaries. Triangles: $N = 216$, truncated octahedral boundaries. The lines are to guide the eye.

furnish the information necessary to compute the elastic constants. We do not give these values here: they are within 20–30% of those previously reported [67], but greater statistical accuracy in the data, particularly for the larger system sizes and the lower values of $k^2$, is required to check

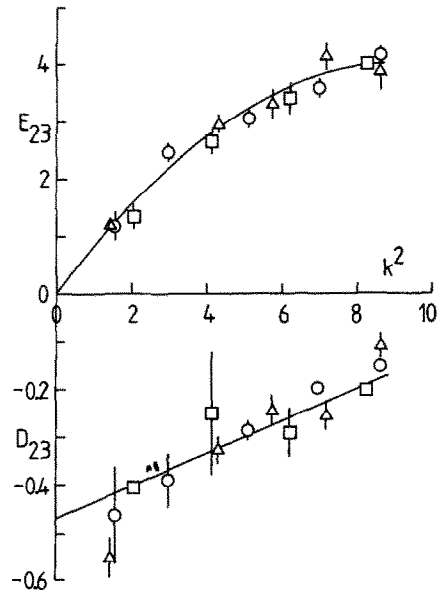


Fig. 11. The functions $E_{23}(k^2, \Delta = 0)$ and $D_{23}(k^2, \Delta = 0)$ for prolate hard ellipsoids with $e = 3$, $\rho/\rho_{cp} = 0.75$ (nematic). Notation as for fig. 10.

for quantitative differences as the system size is varied. In addition, it will be necessary to investigate in more detail the overall dependence of the $E$ and $D$ function on $k^2$ and $\Delta$, rather than simply relying on the $\Delta = 0$ values. However, these preliminary results are very heartening in that they show that the observed finite-$k$ orientational fluctuations are not simply due to, nor strongly dependent upon, the periodic boundary conditions.

## 8. Hard spherocylinders

In the previous sections we have looked at the static and dynamic properties of hard, non-spherical molecules. We found that sufficiently anisometric hard ellipsoids of revolution exhibit many of the static and dynamic properties of real nematogens. Naturally, the question arises whether the nematic phase is the only type of liquid crystal that can be simulated with a hard core model. For instance, one may ask if the excluded-volume effects present in fluids of hard convex particles can induce the formation of a smectic phase, i.e. a fluid that has (at least) one-dimensional translational order, in addition to the orientational order already present in nematics. This question is of some practical interest, as there is recent experimental evidence which shows that smectic ordering takes place in concentrated solutions of rod-like DNA molecules [79].

It seems very likely that hard ellipsoids cannot form a smectic. The reason is the following: smectic phases tend to have a large degree of orientational order. Hence, to a first approximation, we can assume that a smectic consists of perfectly aligned, non-spherical molecules. However, a system consisting of hard ellipsoids of revolution with axial ratio $a/b$, all parallel to the $z$-axis (say), can be mapped onto the hard sphere fluid by a simple scaling of all $z$-coordinates by a factor $b/a$ [80,12]. As hard spheres apparently do not form smectics, parallel hard ellipsoids cannot do so either. So, unless the orientational degrees of freedom stabilize the smectic phase (and this seems unlikely), hard ellipsoids of revolution cannot form smectics.

However, the above scaling argument does not apply to other rod-like molecules. A well-studied example is the hard spherocylinder, i.e. a cylinder of diameter $d$ and length $l$, having hemispherical caps at each end. In fact, recent simulations by Stroobants et al. [81] have shown that a fluid of parallel spherocylinders *does* form a smectic phase when the length-to-width ratio $l/d$ exceeds 0.5. Later, the same authors [82] found that for $l/d \geq 5$ this model system may even exhibit another form of liquid-crystalline order: columnar phases, i.e. liquid crystals where the molecules stack on top of one another to form a two-dimensional lattice of (disordered) columns.

Of course, it may be argued that simulations on a model of parallel hard rods offer only limited insight into the formation of real liquid crystals of rod-like molecules. After all, the orientational degrees of freedom of the molecules have a pronounced effect on the relative stability of the different phases. Until quite recently, there was little direct evidence for the existence of stable nematic, let alone smectic, phases in systems of freely-rotating spherocylinders.

The original MD simulations on spherocylinders by Rebertus and Sando [45] were for $l/d = 1$. This system almost certainly does not form a liquidcrystalline phase. In fact, the pioneering MC calculations on hard spherocylinders by Vieillard-Baron [83] suggest that even for the less spherical case $l/d = 2$, spherocylinders may not have a stable nematic phase. In their MD study

on spherocylinders, Rebertus and Sando could study only very few state points, because of the limited computer power available. However, recent simulations by Frenkel et al. [84,85] indicate that, at least for spherocylinders with $l/d = 5$, a stable smectic phase does indeed exist. In the following sections, we concentrate on the smectic precursor effects and on the dynamics of the smectic phase. Further details about the structural properties may be found elsewhere ([81,82] and op cit.).

### 8.1. The smectic phase

In this section, we describe in some detail the procedures used to establish the existence and stability of the smectic phase for systems of hard parallel spherocylinders, and then proceed to discuss the properties of this phase.

We performed MD simulations on systems of parallel spherocylinders with $l/d$ ratios of 0.25, 0.5, 1 and 5. System sizes varying from 90 to 1080 particles were studied. The structure of the MD program used in these simulations was almost identical to the one used for the simulation of hard ellipsoids. However, as the dynamics of parallel hard spherocylinders is simpler, the spherocylinder-program could handle about twice as many collisions per hour of CPU time. Initially, the system was prepared in a regular close-packed lattice. We prepared this lattice by expanding a close-packed face-centered cubic hard-sphere crystal by a factor $(l/d + 1)$ along the [111] axis. The volume fraction occupied by hard spherocylinders at regular close packing is

$$\eta_{cp} = \frac{\pi}{\sqrt{18}} \frac{1 + (3/2)(l/d)}{1 + \sqrt{3/2}\,(l/d)}. \tag{39}$$

In order to avoid spurious translational order due to incomplete melting, the crystals were expanded to low densities (typically, 30% of close packing), where the solid rapidly melted to form a translationally disordered fluid. Fluid configurations at higher densities were subsequently generated by slow compression (the compression was done in a separate MC run, but the distinction is not essential).

During the runs, the compressibility factor $PV/NkT$ was computed. No discontinuities were observed in the equation-of-state on compressing the spherocylinder fluid. However, for the larger $l/d$ ratios ($l/d \geq 0.5$) the compressibility changes rather suddenly at a density between 40% and 60% of close packing. Snapshots of typical molecular configurations both below and above this "cusp" in the equation of state reveal a pronounced change in the structure of the fluid. At low densities, the fluid is translationally disordered. Then, at a higher density (but well before the freezing point), the fluid orders into parallel layers. However, there is no order within the layers. In other words, the parallel spherocylinder fluid appears to form a smectic-A phase. As there is no (measurable) density jump at this transition to the smectic phase, it seems logical to assume that the phase transition to the smectic phase in continuous, or nearly so. In the vicinity of such a phase transition we may expect to find strong pretransitional fluctuations of the incipient smectic order. As the phase transition is approached, we expect that density fluctuations with a wavelength corresponding to the smectic layer spacing will grow in amplitude, and will decay increasingly slowly. We have therefore computed the longitudinal compo-

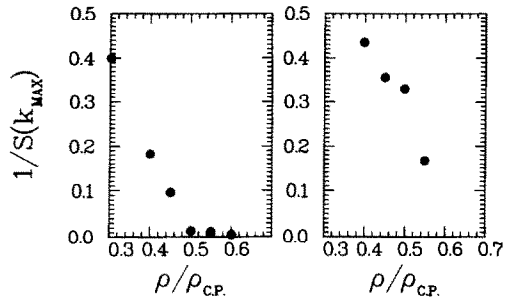


Fig. 12. Density-dependence of the smectic order parameter close to the nematic–smectic transition for hard parallel spherocylinders. We plot the inverse height of the peak $S(k_z)$ at $k_z = k_z^{max}$ as a function of $\rho/\rho_{cp}$. Left: $l/d = 1$. Right: $l/d = 0.25$.

nent of the intermediate scattering function $F(k_z, t)$, defined as

$$F(k_z, t) = \langle \rho(k_z, 0)\rho(-k_z, t)\rangle, \tag{40}$$

where $\rho(k_z, t)$ is the instantaneous amplitude of a longitudinal density fluctuation with wavevector $k_z$. $F(k_z, t = 0)$ is the longitudinal part of the static structure factor, $S(k_z)$, which determines, for instance, the X-ray scattering intensity. Smectic precursor fluctuations will show up as peaks in $S(k_z)$, for values $k_z$ equal to (multiples of) $k_z^{max} \equiv 2\pi/\delta$, where $\delta$ is the spacing of the incipient smectic layers. If the transition to the smectic phase is continuous, the peaks in $S(k_z)$ should diverge at the transition. However, in a simulation on a finite system, the divergence will saturate when the smectic correlation length becomes comparable to the system size. An example of this behaviour is shown in fig. 12. A more sensitive probe of incipient smectic ordering is the critical slowing down of the correlation function $\langle \rho(k_z, 0)\rho(-k_z, t)\rangle$ at $k_z = k_z^{max}$. Measurement of this dynamic quantity makes it possible to distinguish large smectic precursor fluctuations from true (static) smectic ordering, in a finite system. Figure 13 shows how the relaxation rate of smectic precursor fluctuations depends on density. At first, the decay time of $F(k_z^{max}, t)$ decreases with increasing density, because the fluid is less compressible at

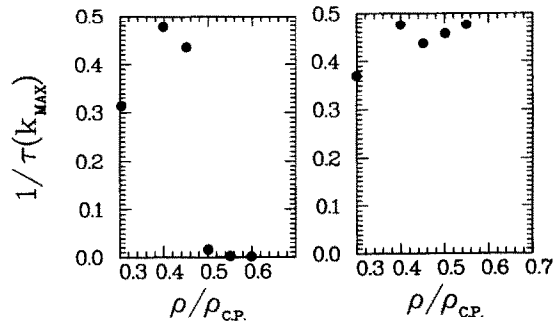


Fig. 13. Relaxation rate of smectic precursor fluctuations close to the nematic–smectic transition for hard parallel spherocylinders. We plot, as a function of $\rho/\rho_{cp}$, the inverse of the relaxation time $\tau(k_z)$ of $F(k_z, t)$ (see eq. (40)) at the peak position $k_z = k_z^{max}$. Left: $l/d = 1$. Right: $l/d = 0.25$.

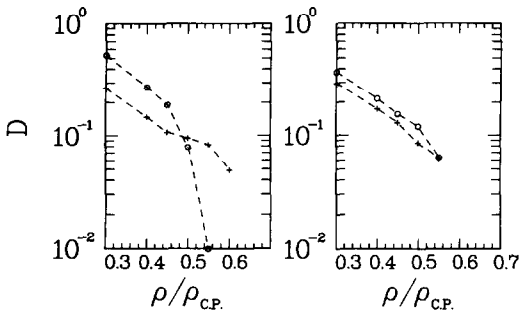


Fig. 14. Diffusion coefficients for the hard parallel spherocylinder fluid in the longitudinal direction, i.e. perpendicular to the smectic layers (circles), and in the transverse direction, parallel to the layers (pluses). Left: $l/d = 1$. Right: $l/d = 0.25$.

higher densities. But beyond a certain density the relaxation rate drops precipitously to zero. This phenomenon provides us with an estimate for the nematic–smectic transition density. For comparison, fig. 13 also shows an example of a fluid which does not become smectic ($l/d = 0.25$). In this case the decay rate of $F(k_z^{\max}, t)$ depends only weakly on density.

The ordering of the fluid in layers has a pronounced effect on the diffusion of individual particles. At low densities, the longitudinal component of the self-diffusion coefficient $D_T^{\parallel}$ is larger than the transverse component $D_T^{\perp}$. This effect is strongest for the most elongated particles. But as smectic layers start to form at higher densities, $D_T^{\parallel}$ decreases much more rapidly than $D_T^{\perp}$. So much so, that in the smectic phase $D_T^{\perp}$ becomes larger than $D_T^{\parallel}$ (see fig. 14). Hence, in the smectic phase, intra-layer diffusion is more rapid than inter-layer diffusion. Incidentally, this effect is also observed in some real liquid crystals [86]. The "phase diagram" of hard parallel spherocylinders as a function of the length-to-width ratio $l/d$ is shown in fig. 15. This phase diagram shows the regions of stability of the nematic, smectic and solid phases as a function of $l/d$. For $l/d > 0.5$, a smectic phase is found between the crystalline solid and the "nematic" fluid. As the non-sphericity of the particles is increased, the smectic range initially

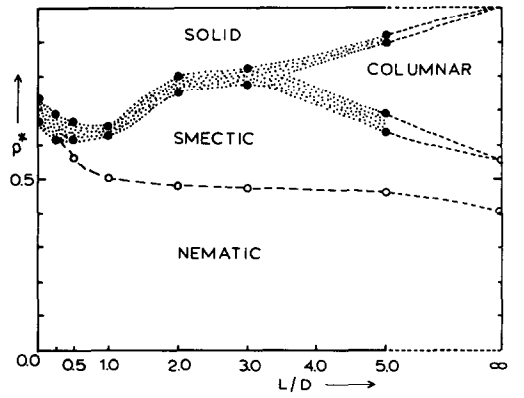


Fig. 15. Phase diagram of the hard parallel spherocylinder fluid. The shaded regions correspond to two-phase coexistence. It should be noted that the precise location of the smectic–columnar transition depends rather strongly on the system size.

grows, but for $3 < l/d < 5$, a columnar liquid-crystalline phase intervenes between the crystalline solid and the smectic phase. For more details, see ref. [82]. It should be stressed that this phase diagram pertains to a system of *parallel* spherocylinders.

Let us next consider spherocylinders with both translational and orientational freedom. What phase diagram should we expect? Clearly, the orientational degrees of freedom will affect the phase diagram in an important way. For instance, at low densities we should now expect an isotropic fluid phase. The question is: What happens at higher densities? Will the orientational freedom destroy the smectic order found in the aligned system? Or will the nematic phase disappear at the expense of the smectic phase? Once again, to find out we resort to numerical simulation.

Simulations on prolate particles with rotational degrees of freedom typically require larger system sizes than simulations on the corresponding system with aligned molecules. The reason is the following. In order to exclude collisions between particles that are not nearest images, the linear dimensions of the simulation box must be at least twice the length of a molecule. This condition puts a practical limitation on the maximum value of $l/d$ that can be simulated, because the volume of the periodic box scales as $L^3$, and hence as $l^3$, while the molecular volume goes as $ld^2$. Hence the minimum number of particles in the periodic box goes as $(l/d)^2$. The simulations reported here were carried out for a system of 576 spherocylinders with $l/d = 5$ in an almost cubic box.

Initially, the spherocylinders were prepared in a regular close-packed lattice as before. The lattice was thereupon expanded to a low density (20% of close packing), but the molecular orientation was kept fixed. We then proceeded in two stages. On the one hand, we carried out a series of simulations in which the spherocylinders were free to rotate. We slowly compressed this orientationally and translationally disordered system until, at $\sim 45\%$ of regular close packing, spontaneous nematic ordering took place. Next, in order to prepare a uniformly aligned nematic, we slowly compressed the *aligned* spherocylinder fluid to 50% of close packing. For an aligned spherocylinder with $l/d = 5$, the transition from the "nematic" low density phase to the smectic phase takes place at 45% of regular close packing. Hence the system thus prepared had smectic order. Next, the molecular orientations were released, and the system was left to equilibrate. During equilibration, the smectic ordering disappeared, while the orientational order persisted (as was to be expected). Thereupon, the system was slowly compressed to see if a smectic phase would form spontaneously. Once again, the most sensitive way to probe the onset of smectic ordering is to study the dynamics of smectic order-parameter fluctuations in the nematic phase. The order in a smectic-A liquid crystal is characterized by a one-dimensional density modulation in the direction of the molecular axes. It is therefore natural to look for pretransitional fluctuations of the Fourier components of the one-particle density, as described above. In fig. 16 the rate of decay of $F(k_x^{\max}, t)$ is plotted as a function of density. As can be seen from the figure, there is a dramatic increase of the lifetime of smectic order-parameter fluctuations with density. Subsequent absolute free energy calculations [85] indicate that a thermodynamically stable smectic phase exists for densities between 60 and 73% of regular close packing. The MD simulations indicate that the nematic-to-smectic (N–S) transition in this system is either continuous, or weakly first-order. In real liquid crystals the nematic to smectic-A transition can be either first-order or continuous. A continuous transition is usually observed if the nematic order parameter at the transition is large. In the present simulations, the nematic order

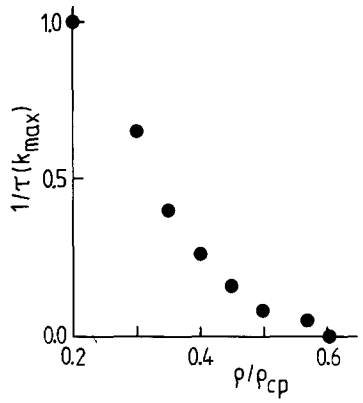


Fig. 16. Relaxation rate of smectic precursor fluctuations for hard, orientationally unconstrained, spherocylinders with $l/d = 5$. We plot, as a function of $\rho/\rho_{cp}$, the inverse of the relaxation time $\tau(k_z)$ of $F(k_z, t)$ (see eq. (40)) at the peak position $k_z = k_z^{max}$.

parameter at the transition is quite large ($S \approx 0.92$; perfect orientational order would correspond to $S = 1$). It therefore seems likely that the N–S phase transition for hard spherocylinders with $l/d = 5$ is continuous.

### 8.2. Elastic constants

In a smectic liquid crystal, the Frank elastic constants $K_2$ and $K_3$ should be infinite. As a nematic liquid crystal approaches a transition to a smectic phase, and assuming that this transition is continuous, it is expected that $K_2$ and $K_3$ should diverge. It is possible that this precursor effect could be observed in a computer simulation. To test this, we have carried out MD simulations for a system of $N = 576$ spherocylinders with length-to-width ratio $l/d = 5$ [67]. The densities corresponding to 45, 50 and 57% of regular close packing. In this density regime, a stable nematic liquid crystal phase was observed, with the nematic order parameter varying from $S = 0.33$ to $S = 0.91$. Frank elastic constants were calculated just as in the case of hard ellipsoids, using the simple fitting procedure which assumed perfect alignment of the director with the simulation box (see sections 5.5 and 7.7). In this case, the length of the runs was less ($\sim 5000 t_c$), and hence the statistical error was larger (10–30%) than for the ellipsoid simulations. The dependence of the Frank elastic constants of the spherocylinder fluid on the nematic order parameter is shown in fig. 17. In the figure, we have also shown the theoretical predictions for a spherocylinder fluid with $l/d = 5$ and $l/d = \infty$ [87,88]. As can be seen from the figure, there is a very large discrepancy between the simulation data and the theoretical predictions for $K_3$. This discrepancy is at least partly due to the failure in the fitting procedure described above. The reason is that, for this spherocylinder system, strong smectic precursor fluctuations occur over most of the nematic range (see section 8.1). In order to obtain a reliable estimate of $K_3$, it is important to use only $\boldsymbol{k}$-values such that $k_z \ll 2\pi/\xi$, where $\xi$ is the (longitudinal) correlation length of smectic order-parameter fluctuations. In practice it turns out that, for the system size under consideration, there are simply not enough low $k_z$ values available to construct such a fit.

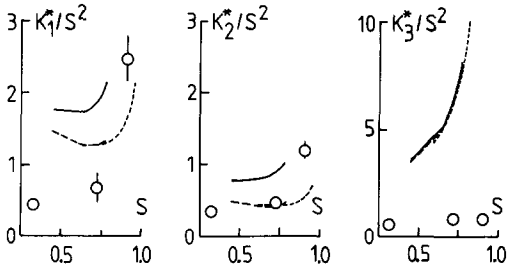


Fig. 17. Dependence of Frank elastic constants of the hard spherocylinder fluid on nematic order parameter $S$. We plot $K_1^*/S^2$, $K_2^*/S^2$ and $K_3^*/S^2$ where $K_i^* = K_i d/k_B T$ for systems with $l/d = 5$. We compare with theoretical predictions based on data from the following. Solid line: ref. [87], $l/d = 5$. Long dashes: ref. [87], $l/d = \infty$. Short dashes: ref. [88], $l/d = \infty$.

It is disappointing, but not totally unexpected, to see no evidence of divergent elastic constants close to the N–S transition. The relevant correlation lengths may well be much larger than the system size employed here.

### 8.3. Collective rotation

We close this section with a discussion of collective rotation in the *isotropic* phase of the spherocylinder fluid. As in the case of ellipsoids, a kinetic theory prediction exists [17,77,78] for the value of the dynamic correlation factor $j_2$ for spherocylinders at low density:

$$1 + j_2 \approx \frac{1}{1 + 9/\left(32 + 24(l/d) + 2(l/d)^2\right)}. \tag{41}$$

We have also investigated the behaviour of $j_2$ for hard spherocylinders with $l/d = 5$. For this system, kinetic theory predicts that $j_2$ should be small and negative, just as for the prolate hard ellipsoids discussed in section 7.6. If we assume that we can use the low density theory, then the predicted value is $j_2 \approx -0.04$. However, for the spherocylinders we appear to observe pronounced deviations from the low-density kinetic theory. To be precise, at low densities (i.e. 20%of regular close packing) we find that $j_2 \approx -0.06$ (see table 3) which is compatible with the (low-density) kinetic theory. However, at higher densities we find clear evidence that $j_2$ change sign and increases with increasing density. At $\rho/\rho_{cp} = 0.40$, i.e. the highest density at which we

Table 3
Static and dynamic orientational correlations for hard spherocylinders

| $\rho/\rho_{cp}$ | $1 + g_2$ | $\tau_c$ | $1 + j_2$ |
|---|---|---|---|
| 0.20 | 1.22 | 2.32 | 0.94 |
| 0.30 | 1.64 | 4.12 | 1.41 |
| 0.35 | 2.62 | 9.06 | 1.50 |
| 0.40 | 2.64 | 11.6 | 1.63 |

could determine it, $j_2$ had risen to 0.6. Although the data are noisy, we found no evidence for this type of increase in the case of hard ellipsoids (see fig. 9). At present, the reason why the collective orientational dynamics of ellipsoids and spherocylinders should behave so differently is not at all clear.

## 9. Hard dumb-bells

### 9.1. Computer code

The fused hard sphere or hard dumb-bell model consists of two spherical atoms, diameter $\sigma$, with a distance $l$ between the centres. Consequently, the condition of overlap of two molecules $i$, $j$, is simply a combination of hard sphere overlap criteria, namely $r_{iajb}^2 < \sigma^2$ for any $a$, $b$, where $\boldsymbol{r}_{iajb} = \boldsymbol{r}_{ia} - \boldsymbol{r}_{jb}$ and $a$, $b = 1, 2$ label the atoms. Once two molecules are known to be touching, it is a simple matter to locate the point of contact on the appropriate spherical surfaces. We use this case to illustrate the calculation of the time of collision, and the implementation of collision dynamics, for a pair of molecules.

To solve the collision time equation, eq. (9), by a standard combination of the Newton–Raphson method with interval bisection [40], we require a routine that provides both the overlap function $f_{ij}(t)$ and its time derivative $d_{ij}(t) \equiv \dot{f}_{ij}(t)$ as functions of time $t$. We pass into the routine, through a COMMON block, information about the colliding pair at some fixed time $t_0$ (typically the end of a timestep). This would include relative positions and velocities, $\boldsymbol{r}_{ij} \equiv \boldsymbol{r}_i - \boldsymbol{r}_j$, $\boldsymbol{v}_{ij} \equiv \boldsymbol{v}_i - \boldsymbol{v}_j$, as well as the orientations and angular velocities at that time. The names of variables referring to time $t_0$ are identified with a 0 here.

```
      COMMON/IJPAIR/RXIJ0,RYIJ0,RZIJ0,
     :      VXIJ,VYIJ,VZIJ,
     :      UXI0,UYI0,UZI0,
     :      OXI,OYI,OZI,OMI,AL2,
     :      UXJ0,UYJ0,UZJ0,
     :      OXJ,OYJ,OZJ,OMJ,BL2,T0
```

The variables AL2 and BL2 are equal to $\pm l/2$, where $l$ is the distance between the hard sphere atomic centres of the dumb-bell. Depending on the signs, these variables identify which of the two atoms on each molecule are being considered. The first step is to adjust the configurational variables so that they refer to molecules at time $t$ instead of $t_0$. This code is similar to that given in section 4.1. The new position and orientation variable names end with T instead of 0.

```
      DT = T - T0

      RXIJT  = RXIJ0 + VXIJ*DT
      RYIJT  = RYIJ0 + VYIJ*DT
      RZIJT  = RZIJ0 + VZIJ*DT
```

```
OMT    = OMI*DT
COSOMT = COS(OMT)
SINOMT = SIN(OMT)
OUX    = OYI*UZI0 - OZI*UYI0
OUY    = OZI*OXI0 - ZXI*UZI0
OUZ    = OXI*UYI0 - OYI*UXI0
UXIT   = UXI0*COSOMT + OUX*SINOMT
UYIT   = UYI0*COSOMT + OUY*SINOMT
UZIT   = UZI0*COSOMT + OUZ*SINOMT
DUXIT  = OMI*(OUX*COSOMT - UXI0*SINOMT)
DUYIT  = OMI*(OUY*COSOMT - UYI0*SINOMT)
DUZIT  = OMI*(OUZ*COSOMT - UZI0*SINOMT)

OMT    = OMJ*DT
COSOMT = COS(OMT)
SINOMT = SIN(OMT)
OUX    = OYJ*UZJ0 - OZJ*UYJ0
OUY    = OZJ*UXJ0 - OXJ*UZJ0
OUZ    = OXJ*UYJ0 - OYJ*UXJ0
UXJT   = UXJ0*COSOMT + OUX*SINOMT
UYJT   = UYJ0*COSOMT + OUY*SINOMT
UZJT   = UZJ0*COSOMT + OUZ*SINOMT
DUXJT  = OMJ*(OUX*COSOMT - UXJ0*SINOMT)
DUYJT  = OMJ*(OUY*COSOMT - UYJ0*SINOMT)
DUZJT  = OMJ*(OUZ*COSOMT - UZJ0*SINOMT)

RXABT  = RXIJT + AL2*UXIT - BL2*UXJT
RYABT  = RYIJT + AL2*UYIT - BL2*UYJT
RZABT  = RZIJT + AL2*UZIT - BL2*UZJT

RXABT  = RXABT - ANINT(RXABT)
RYABT  = RYABT - ANINT(RYABT)
RZABT  = RZABT - ANINT(RZABT)

VXABT  = VXIJ + AL2*DUXIT - BL2*DUXJT
VYABT  = VYIJ + AL2*DUYIT - BL2*DUYJT
VZABT  = VZIJ + AL2*DUZIT - BL2*DUZJT
FIJ    = RXABT**2 + RYABT**2 + RZABT**2 - SIGSQ
DIJ    = 2.0*(RXABT*VXABT + RYABT*VYABT
:              + RZABT*VZABT)
```

We require time-derivative values (DUXIT, etc.) as well as positions and orientations at time $t$. The variables RXABT, RYABT, RZABT store $r_{ia\,jb}(t)$. In this example, we apply the minimum

image correction for a cubic box of unit side. The new values and their time derivatives are used in the calculation of $f_{ij}(t)$ and $d_{ij}(t)$ (the variable SIGSQ stores $\sigma^2$).

To implement the collision dynamics equations, eqs. (10)–(13), the computer code is given below. We assume that the colliding pair has been moved to the point of collision, with the collision time determined by the Newton–Raphson method. The centre–centre distance is stored in RXIJ, RYIJ, RZIJ as usual. The first step is to convert the unit vectors pointing along the symmetry axis into proper vectors giving the atomic sphere positions relative to the molecular centres. These are then used to calculate the vector $\boldsymbol{r}_{iajb}$.

```
AXI  = UXI*AL2
AYI  = UYI*AL2
AZI  = UZI*AL2
BXJ  = UXI*BL2
BYJ  = UYJ*BL2
BZJ  = UZJ*BL2

RXAB = RXIJ + AXI - BXJ
RYAB = RYIJ + AYI - BYJ
RZAB = RZIJ + AZI - BZJ
RXAB = RXAB - ANINT(RXAB)
RYAB = RYAB - ANINT(RYAB)
RZAB = RZAB - ANINT(RZAB)
```

Once again, cubic periodic boundaries in a box of unit side are assumed. The position of the contact point relative to the centre of each molecule, $\boldsymbol{r}_{ci}$, $\boldsymbol{r}_{cj}$, and the normal to the touching surfaces, $\boldsymbol{n}$, are then determined (see section 4.4).

```
RXCI = AXI - 0.5*RXAB
RYCI = AYI - 0.5*RYAB
RZCI = AZI - 0.5*RZAB
RXCJ = BXJ + 0.5*RXAB
RYCJ = BYJ + 0.5*RYAB
RZCJ = BZJ + 0.5*RZAB

NXI  = RXAB/SIGMA
NYI  = RYAB/SIGMA
NZI  = RZAB/SIGMA
```

The next step is the calculation of the collisional impulse according to eq. (13). Remember that we store angular velocities as unit vectors (in OXI, OYI, OZI, etc.) and magnitudes (in OMI) separately.

```
VXIJ  = VXI - VXJ
VYIJ  = VYI - VYJ
VZIJ  = VZI - VZJ
```

```
OXI    = OXI*OMI
OYI    = OYI*OMI
OZI    = OZI*OMI
OXJ    = OXJ*OMJ
OYJ    = OYJ*OMJ
OZJ    = OZJ*OMJ
GXIJ   = VXIJ + OYI*RZCI - OZI*RYCI
:      - OYJ*RZCJ + OZJ*RYCJ
GYIJ   = VYIJ + OZI*RXCI - OXI*RZCI
:      - OZJ*RXCJ + OXJ*RZCJ
GZIJ   = VZIJ + OXI*RYCI - OYI*RXCI
:      - OXJ*RYCJ + OYJ*RXCJ
GN     = NXI*GXIJ + NYI*GYIJ + NZI*GZIJ
SUMSQ  = RXCI**2 + RYCI**2 + RZCI**2
:      + RXCJ**2 + RYCJ**2 + RZCJ**2
:      - (NXI*RXCI + NYI*RYCI + NZI*RZCI)**2
:      - (NXI*RXCJ + NYI*RYCJ + NZI*RZCJ)**2
IMP    = -GN/((1.0/MASS) + 0.5*SUMSQ/INERT)
IMPX   = IMP*NXI
IMPY   = IMP*NYI
IMPZ   = IMP*NZI
```

Finally, velocities and angular velocities are updated according to eq. (10), with the molecular mass and moment of inertia divided out as appropriate.

```
VXI  = VXI + IMPX/MASS
VYI  = VYI + IMPY/MASS
VZI  = VZI + IMPZ/MASS
VXJ  = VXJ - IMPX/MASS
VYJ  = VYJ - IMPY/MASS
VZJ  = VZJ - IMPZ/MASS
OXI  = OXI + (RYCI*IMPZ - RZCI*IMPY)/INERT
OYI  = OYI + (RZCI*IMPX - RXCI*IMPZ)/INERT
OZI  = OZI + (RXCI*IMPY - RYCI*IMPX)/INERT
OXJ  = OXJ - (RYCJ*IMPZ - RZCJ*IMPY)/INERT
OYJ  = OYJ - (RZCJ*IMPX - RXCJ*IMPZ)/INERT
OZJ  = OZJ - (RXCJ*IMPY - RYCJ*IMPX)/INERT
OMI  = SQRT(OXI**2 + OYI**2 + OZI**2)
OXI  = OXI/OMI
OYI  = OYI/OMI
OZI  = OZI/OMI
OMJ  = SQRT(OXJ**2 + OYJ**2 + OZJ**2)
OXJ  = OXJ/OMJ
OYJ  = OYJ/OMJ
OZJ  = OZJ/OMJ
```

### 9.2. Rigid vs. non-rigid molecules

The hard dumb-bell model provides an opportunity to compare a system having a completely rigid interatomic bond with one in which some bond length variation is allowed, as discussed in section 3.4. To our knowledge, the only comparison utilizing MD methods for both rigid and non-rigid dumb-bells appeared in a brief report of Bellemans and co-workers [38] for the two-dimensional case. These results indicated that the "rattling bond" model reproduced the equation of state of the rigid dumb-bells quite accurately, and efficiently, with suitably chosen limits on the allowed bond-length variation. Since that time, Chapela and co-workers [39] have compared MD simulations of the non-rigid molecules with MC results for their rigid counterparts. The MD simulations satisfactorily reproduce the structural features seen by MC. Recently, we have started to apply MD to both types of model, so as to compare in more detail the dynamical properties in the rigid and non-rigid cases.

To illustrate this, we present here results for hard dumb-bells with atomic diameter $\sigma$ taken as a unit of length, distance $l/\sigma = 0.6$ between the atomic centres, at a molecular density $\rho\sigma^3 = 0.5$. Our system size is $N = 108$ molecules. The rigid-molecule MD program used the retrospective collision handling procedure described in sections 4.3 and 9.1. The non-rigid-molecule program used conventional collision-by-collision dynamics as described in section 3. In each case, identical Verlet-type neighbour lists based on the atoms were used to speed up the program. In table 4 we compare the rigid model results with the non-rigid case for maximum bond-length variations $\delta l = 0.1, 0.05, 0.02, 0.01$, respectively. For runs of the same length in simulation time, we give the cpu time used (on a VAX 11/750 with floating point accelerator), the total number of collisions, and the breakdown of this quantity into "external" or intermolecular contributions and the two types of intramolecular collision, namely attractive ("well") and repulsive ("wall"). We compare program speeds in terms of intermolecular collisions per unit cpu time. In table 5 we also give the various contributions to the pressure arising from these sources. As expected, the intramolecular collisions become dominant as the "rattling" bond is tightened up, but their contributions to quantities such as the pressure tend to cancel. The computer time spent on these internal collisions makes the simulation program less efficient for $\delta l = 0.01$ than for the rigid molecule case; however, the efficiency is greater for the larger values of $\delta l$, and even $\delta l = 0.05$ seems quite a satisfactory value for predicting the pressure. This confirms the conclusions of

Table 4
Rigid and non-rigid dumb-bell collisions

| $\delta l$ | Collisions | | | | CPU time (s) | Speed |
|---|---|---|---|---|---|---|
| | total | wall | well | external | | |
| 0.1 | 60935 | 15951 | 8949 | 36035 | 12065 | 2.99 |
| 0.05 | 85937 | 28344 | 21299 | 36294 | 15759 | 2.30 |
| 0.02 | 158796 | 64596 | 57708 | 36492 | 26829 | 1.36 |
| 0.01 | 278967 | 124896 | 117870 | 36201 | 45495 | 0.80 |
| 0 | 33915 | – | – | 33915 | 28923 | 1.17 |

Table 5
Rigid and non-rigid dumb-bell pressures

| $\delta l$ | $PV/Nk_BT$ contributions | | | | |
|---|---|---|---|---|---|
| | total | wall | well | external | ideal |
| 0.1 | 12.67 | 2.40 | −1.59 | 9.87 | 2.0 |
| 0.05 | 12.77 | 4.50 | −3.67 | 9.94 | 2.0 |
| 0.02 | 12.79 | 10.43 | −9.63 | 9.99 | 2.0 |
| 0.01 | 12.79 | 20.18 | −19.35 | 9.96 | 2.0 |
| 0 | 12.86 | – | – | 11.86 | 1.0 |

Chapela et al. [39]. Interestingly, however, the pressure in the rigid dumb-bell case is slightly higher than would be predicted by extrapolating the non-rigid values to the limit $\delta l = 0$.

In fig. 18 we show the atomic velocity autocorrelation function for the rigid model and the various non-rigid approximations. We have left these functions unnormalized: with our chosen scale (unit temperature and atomic mass) the initial value $\langle v_i^2 \rangle$ for atoms in the non-rigid model is equal to 3 while that in the rigid model is 2.5, corresponding to one degree of freedom fewer per molecule. Nonetheless, the curves for the non-rigid case rapidly approach that for the rigid dumb-bell, in a decaying oscillatory fashion, with the period of oscillation decreasing as the parameter $\delta l$ decreases. Thus, the internal degree of freedom equilibrates more-or-less rapidly, leaving the atomic correlations at long time almost unaffected. Dynamical quantities reflecting the transfer of energy between internal and external modes will also highlight the differences between the non-rigid models with different $\delta l$ parameters and between these models and their rigid counterpart. However, many dynamical properties, such as the centre-of-mass velocity autocorrelation function, and orientational correlation functions as defined in eq. (19), are relatively insensitive to the degree of non-rigidity. Further discussion of these results may be found elsewhere [89].

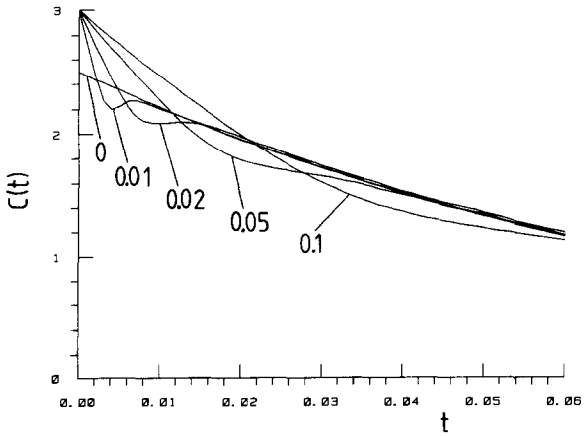


Fig. 18. Atomic velocity autocorrelation for rigid ($\delta l = 0$) and non-rigid ($\delta l = 0.01, 0.02, 0.05, 0.1$) hard dumb-bells.

## 10. Look forward

In pursuing the current line of research, we have stuck to the principle of studying the properties of simple systems as fully as possible, the better to comprehend the behaviour of more complicated ones. Clearly, even molecular models as simple as the ones discussed here exhibit a rich variety of behaviour. Moreover, they should function as useful reference systems for perturbation theories or modified kinetic theories involving more realistic interactions.

As we have seen, the phase behaviour and dynamical properties of hard particle systems are extremely dependent on the shape. In the future, there is no reason to restrict ourselves to ellipsoids or spherocylinders. All convex bodies can be defined in terms of a "support function", and it may be possible to develop procedures to calculate this function, and hence the shape of a reference hard convex body, from quantum mechanical constant-energy surfaces.

Considerable progress has been made recently in the development of theories for the structural properties of bulk fluids, although much remains to be done. Simulations will undoubtedly continue to play a vital role in the forseeable future, in helping to refine and develop these theories. The same is true for the dynamical properties where the theory, especially for anisometric bodies, is in its infancy. Of course, these remarks apply *a forteriori* to the more "exotic" phases such as the nematic, smectic and columnar. Studies of hard particle systems have proved a fascinating adventure into the unknown. Who knows how many more surprises are in store?

## Acknowledgements

It is a pleasure to thank our collaborators, Glenn Evans and Dan Kivelson, for their contribution to much of the work reported here. This research has been supported by the National Science Foundation (NSF), by the Petroleum Research Fund through grant PRF 18122-AC6 and by the Science and Engineering Research Council (SERC). The work of the FOM Institute is part of the research program of FOM and is supported by the "Nederlandse Organisatie voor Wetenschappelijk Onderzoek" (NWO). Computational facilities were provided at the John von Neumann Center for Scientific Computing at Princeton NJ, at the University of Manchester Regional Computer Centre, and at the Amsterdam computer center (SARA), funded by NSF, SERC and WGS, respectively. International travel was made possible by a travel award from NATO.

## References

[1] B.J. Alder and T.E. Wainwright, J. Chem. Phys. 27 (1957) 1208.
[2] B.J. Alder and T.E. Wainwright, J. Chem. Phys. 31 (1959) 459.
[3] B.J. Alder and T.E. Wainwright, J. Chem. Phys. 33 (1960) 1439.
[4] B.J. Alder and T.E. Wainwright, Phys. Rev. 127 (1962) 359.
[5] G.C. Maitland, M. Rigby, E.B. Smith and W.A. Wakeham, Intermolecular Forces: their Origin and Determination (Clarendon Press, Oxford, 1981).
[6] R. Car and M. Parrinello, Phys. Rev. Lett. 55 (1985) 2471.

[7] J.P. Hansen and I.R. McDonald, Theory of Simple Liquids, 2nd ed. (Academic Press, London, 1986).
[8] B.J. Alder, D.M. Gass and T.E. Wainwright, J. Chem. Phys. 53 (1970) 3813.
[9] B.J. Alder and T.E. Wainwright, Phys. Rev. A1 (1970) 18.
[10] D. Levesque, J.J. Weis and J.P. Hansen, in: Applications of the Monte Carlo Method in Statistical Physics, Topics in Current Physics 36, 2nd ed., K. Binder (Springer, Berlin, 1987) chap. 2.
[11] T. Boublik and I. Nezbeda, Collection Czech. Chem. Commun. 51 (1986) 2301.
[12] J.A. Barker and D. Henderson, Rev. Mod. Phys. 48 (1976) 587.
[13] C.G. Gray and K.E. Gubbins, The Theory of Molecular Fluids. II. Applications (Clarendon Press, Oxford, to be published) appendix 6A.
[14] M. Wertheim, private communication.
[15] R.D. Levine and R.B. Bernstein, Molecular Reaction Dynamics and Chemical Reactivity (Oxford University Press, Oxford, 1987).
[16] D. Frenkel, Mol. Phys. 60 (1987) 1.
[17] R.G. Cole and G.T. Evans, Ann. Rev. Phys. Chem. 37 (1986) 105.
[18] R. Eppenga and D. Frenkel, Mol. Phys. 52 (1984) 1303.
[19] J. Kolafa, Mol. Phys. 63 (1988) 559.
[20] A.Z. Panagiotopoulos, Mol. Phys. 61 (1987) 813.
[21] H.C. Andersen, J. Chem. Phys. 72 (1980) 2384.
[22] Ph. De Smedt, J. Talbot and J.L. Lebowitz, Mol. Phys. 59 (1986) 625.
[23] J. O'Dell and B.J. Berne, J. Chem. Phys. 63 (1975) 2376.
[24] G. Subramanian and H.T. Davis, Phys. Rev. A 11 (1975) 1430.
[25] B.J. Berne, J. Chem. Phys. 66 (1977) 2821.
[26] C.S. Pangali and B.J. Berne, J. Chem. Phys. 67 (1977) 4571.
[27] J.W. Lyklema, Physica A 96 (1979) 573.
[28] J.J. Erpenbeck and W.W. Wood, in: Statistical Mechanics B, ed. B.J. Berne (Plenum, New York, 1977) 1.
[29] M.P. Allen and D.J. Tildesley, Computer Simulation of Liquids (Oxford University Press, Oxford, 1987).
[30] L. Verlet, Phys. Rev. 159 (1967) 98.
[31] B. Quentrec and C. Brot, J. Comput. Phys. 13 (1975) 430.
[32] R.W. Hockney and J.W. Eastwood, Computer Simulation Using Particles (McGraw-Hill, New York, 1981).
[33] D.C. Rapaport, J. Comput. Phys. 34 (1980) 184.
[34] D.C. Rapaport, Comput. Phys. Rep. 9 (1988) 1.
[35] D. Frenkel and J.F. Maguire, Mol. Phys. 49 (1983) 503.
[36] D.C. Rapaport, J. Phys. A 11 (1978) L213.
[37] D.C. Rapaport, J. Chem. Phys. 71 (1979) 3299.
[38] A. Bellemans, J. Orban and D. van Belle, Mol. Phys. 39 (1980) 781.
[39] G.A. Chapela, S.E. Martinez-Casas and J. Alejandre, Mol. Phys. 53 (1984) 139.
[40] W.H. Press, B.P. Flannery, S.A. Teukolsky and W.T. Vetterling, Numerical Recipes (Cambridge University Press, Cambridge, 1986).
[41] M.P. Allen and A.A. Imbierski, Mol. Phys. 60 (1987) 453.
[42] J.J. Magda, H.T. Davis and M. Tirell, J. Chem. Phys. 85 (1986) 6674.
[43] M.P. Allen and I.C.H. Cunningham, Mol. Phys. 58 (1986) 615.
[44] J.J. Magda, H.T. Davis and M. Tirrell, J. Chem. Phys. 88 (1988) 1207.
[45] D.W. Rebertus and K.M. Sando, J. Chem. Phys. 67 (1977) 2585.
[46] R.M. Stratt, S.L. Holmgren and D. Chandler, Mol. Phys. 42 (1981) 1233.
[47] W.J. McNeill and W.G. Madden, J. Chem. Phys. 76 (1982) 6221.
[48] M. Doi and S.F. Edwards, J. Chem. Soc. Faraday Trans. II 74 (1978) 560.
[49] L.J. Lowden and D. Chandler, J. Chem. Phys. 61 (1974) 5228.
[50] C.G. Gray and K.E. Gubbins, The Theory of Molecular Fluids. I. Fundamentals (Clarendon Press, Oxford, 1984).
[51] W.B. Streett and D.J. Tildesley, Proc. Roy. Soc. Lond. A 348 (1976) 485.
[52] A. Perera, P.G. Kusalik and G.N. Patey, J. Chem. Phys. 87 (1987) 1295.
[53] V.N. Kabadi and W.A. Steele, Ber. Bunsenges. Phys. Chem. 89 (1985) 2.

[54] F. Ghazi and M. Rigby, Mol. Phys. 62 (1987) 1103.
[55] B.J. Berne and J.A. Montgomery, Mol. Phys. 32 (1976) 363.
[56] R.M. Lynden-Bell, in: Molecular Liquids, Dynamics and Interactions, eds. A.J. Barnes, W.J. Orville-Thomas and J. Yarwood, NATO ASI series 135 (Reidel, Dordrecht, 1984) p. 501.
[57] F.C. Frank, Discuss. Faraday Soc. 25 (1958) 19.
[58] P.G. de Gennes, The Physics of Liquid Crystals. (Clarendon Press, Oxford, 1974).
[59] D. Forster, Ann. Phys. 85 (1974) 505.
[60] J. Vieillard-Baron, J. Chem. Phys. 56 (1972) 4729.
[61] D. Frenkel, B.M. Mulder and J.P. McTague, Phys. Rev. Lett. 52 (1984) 287.
[62] J.W. Perram, M.S. Wertheim, J.L. Lebowitz and G.O. Williams, Chem. Phys. Lett. 105 (1984) 277.
[63] D. Frenkel and B.M. Mulder, Mol. Phys. 55 (1985) 1171.
[64] J.W. Perram and M.S. Wertheim, J. Comput. Phys. 58 (1985) 409.
[65] M.P. Allen and D. Frenkel, Phys. Rev. Lett. 58 (1987) 1748.
[66] M.P. Allen, Molecular Simulation 2 (1989) 301.
[67] M.P. Allen and D. Frenkel, Phys. Rev. A 37 (1988) 1813.
[68] J. Talbot, M.P. Allen, G.T. Evans, D. Frenkel and D. Kivelson, Phys. Rev. A, to appear.
[69] W.W. Wood, in: Fundamental Problems in Statistical Mechanics. III ed. E.G.D. Cohen (North-Holland, Amsterdam, 1975) p. 331.
[70] M. Wertheim and J. Talbot, in preparation.
[71] J. Talbot, M.P. Allen, G.T. Evans, D. Frenkel and D. Kivelson, in preparation.
[72] T. Keyes and D. Kivelson, J. Chem. Phys. 56 (1974) 1057.
[73] For a discussion, see: D. Kivelson and P.A. Madden, Ann. Rev. Phys. Chem. 31 (1980) 523.
[74] G.R. Alms, T.D. Gierke and W.H. Flygare, J. Chem. Phys. 61 (1974) 4083.
T.D. Gierke and W.H. Flygare, J. Chem. Phys. 61 (1974) 2231.
[75] T.I. Cox, M.R. Battaglia and P.A. Madden, Mol. Phys. 38 (1979) 1539.
[76] P.A. Madden, M.R. Battaglia, T.I. Cox, R.K. Pierens and J. Champion, Chem. Phys. Lett. 76 (1980) 604; Mol. Phys. 38 (1979) 1539.
[77] G.T. Evans, R.G. Cole and D.K. Hoffman, J. Chem. Phys. 77 (1982) 3209.
[78] G.T. Evans and D.R. Evans, J. Chem. Phys. 81 (1984) 6039.
[79] T.E. Strzelecka, M.W. Davidson and R.L. Rill, Nature 331 (1988) 457.
[80] J.L. Lebowitz and J.W. Perram, Mol. Phys. 50 (1983) 1207.
[81] A. Stroobants, H.N.W. Lekkerkerker and D. Frenkel, Phys. Rev. Lett. 57 (1986) 1452.
[82] A. Stroobants, H.N.W. Lekkerkerker and D. Frenkel, Phys. Rev. A 36 (1987) 2929.
[83] J. Vieillard-Baron, Mol. Phys. 28 (1974) 809.
[84] D. Frenkel, J. Phys. Chem. 91 (1987) 4912.
[85] D. Frenkel, H.N.W. Lekkerkerker and A. Stroobants, Nature 332 (1988) 822.
[86] M. Hara, H. Tenmei, S. Ichikawa, H. Takezoe and A. Fukuda, Jap. J. Appl. Phys. 24 (1985) L777.
[87] A. Poniwierski and J. Stecki, Mol. Phys. 38 (1979) 249.
[88] S.D. Lee and R.B. Meyer, J. Chem. Phys. 84 (1986) 3443.
[89] M.P. Allen, Molecular Simulation, to appear.